PCCP

(De)lithiation of Spinel Ferrites Fe3O4, MgFe2O4, and ZnFe2O4: A Combined Spectroscopic, Diffraction and Theory Study

Journal:	*Physical Chemistry Chemical Physics*
Manuscript ID	CP-ART-04-2020-002322.R1
Article Type:	Paper
Date Submitted by the Author:	11-Aug-2020
Complete List of Authors:	Bock, David; Stony Brook University, Chemistry Tallman, Killian; SUNY Stony Brook Guo, Haoyue; Stony Brook University, Chemistry; Brookhaven National Laboratory, Chemistry Quilty, Calvin; Stony Brook University Yan, Shan; Brookhaven National Laboratory Smith, Paul; Valparaiso University, Chemistry Zhang, Bingjie; Department of Chemistry, Stony Brook University, Stony Brook, New York, U.S.A., chemistry Lutz, Diana; Stony Brook University, Chemistry McCarthy, Alison; SUNY Stony Brook Huie, Matthew; SUNY Stony Brook Burnett, Veronica; SUNY Stony Brook Bruck, Andrea; Stony Brook University, Marschilok, Amy; Stony Brook University, Materials Science and Engineering Takeuchi, Esther; Stony Brook University, Materials Science and Engineering Liu, Ping; Brookhaven National Lab, Chemistry Takeuchi, Kenneth; Stony Brook University, Chemistry

ARTICLE

(De)lithiation of Spinel Ferrites Fe_3O_4, $MgFe_2O_4$, and $ZnFe_2O_4$: A Combined Spectroscopic, Diffraction and Theory Study

Received 00th January 20xx,
Accepted 00th January 20xx

DOI: 10.1039/x0xx00000x

David C. Bock[1,†], Killian R. Tallman[2,†], Haoyue Guo[2], Calvin Quilty[2], Shan Yan[1], Paul F. Smith[2,3], Bingjie Zhang[2], Diana M. Lutz[2,5,6], Alison H. McCarthy[4,7,8], Matthew M. Huie[4], Veronica Burnett[4], Andrea M. Bruck[2], Amy C. Marschilok[1,2,4], Esther S. Takeuchi[1,2,4], Ping Liu[1], and Kenneth J. Takeuchi[2,4]*

Iron based materials hold promise as next generation battery electrode materials for Li ion batteries due to their earth abundance, low cost, and low environmental impact. The iron oxide, magnetite Fe_3O_4, adopts the spinel (AB_2O_4) structure. Other +2 cation transition metal centers can also occupy both tetrahedral and/or octahedral sites in the spinel structure including $MgFe_2O_4$, a partially inverse spinel, and $ZnFe_2O_4$, a normal spinel. Though structurally similar to Fe_3O_4 in the pristine state, previous studies suggest significant differences in structural evolution depending on the +2 cation in the structure. This investigation involves X-ray absorption spectroscopy and X-ray diffraction affirmed by density function theory (DFT) to elucidate the role of the +2 cation on the structural evolution and phase transformations during de(lithiation) of the spinel ferrites Fe_3O_4, $MgFe_2O_4$, $ZnFe_2O_4$. The cation in the inverse, normal and partially inverse spinel structures located in the tetrahedral (8a) site migrates to the previously unoccupied octahedral 16c site by 2 electron equivalents of lithiation, resulting in a disordered $[A]_{16c}[B_2]_{16d}O_4$ structure. DFT calculations support the experimental results, predicting full displacement of the 8a cation to the 16c site at 2 electron equivalents. Substitution of the +2 cation results in segregation of oxidized phases in the charged state. This report provides significant structural insight into the (de)lithiation mechanisms for an intriguing class of iron oxide materials.

Introduction

Iron oxides hold promise for future battery applications due to their natural abundance, low cost, and the opportunity for high lithium storage capacity.[1] Iron oxide readily can adopt the spinel (AB_2O_4) structure (**Figure 1**) as magnetite, (Fe_3O_4), an inverse spinel with Fe^{3+} preferentially occupying tetrahedral sites (Wyckoff position 8a), and Fe^{2+} and Fe^{3+} occupying octahedral sites (16d) in a cubic close packed array of O^{2-} ions (site 32e). Two vacant octahedral sites exist per formula unit. Lithium ions can be introduced either chemically or electrochemically into the Fe_3O_4 structure at room temperature.[2] Full lithiation of Fe_3O_4 results in conversion of the oxide to Fe metal and Li_2O, with a corresponding theoretical capacity of 924 mAh/g. The reduction process is complex, with multiple phase transformations occurring that are dependent on the electrochemical conditions and the crystallite size of the active material.[3, 4] With appropriate crystallite size of the parent Fe_3O_4 material, electrochemical reversibility is enabled by maintenance of the ccp oxygen framework throughout the (de)lithiation processes.[4]

While extensive work has been done to improve the electrochemical function of Fe_3O_4,[1, 5-7] the opportunity also exists to pair iron with other metals that are amenable to the spinel structure, where the second metal exists as a +2 cation and can occupy both tetrahedral and/or octahedral sites. These materials include magnesium ferrite, $MgFe_2O_4$, and zinc ferrite, $ZnFe_2O_4$. Though structurally similar to Fe_3O_4 in the pristine state, previous studies[8, 9] suggest significant differences in delivered capacity and structural evolution depending on the +2 cation in the structure. In the case of $ZnFe_2O_4$, the pristine structure is that of a normal spinel, with Zn^{2+} in tetrahedral sites (8a) and Fe^{3+} in octahedral sites (16d). The theoretical capacity of the materials is 889 mAh/g, assuming full reduction to Fe^0 and Zn^0. Studies of the discharge mechanism of $ZnFe_2O_4$ have recently been reported to characterize the (de)lithiation intermediates.[10, 11] It was determined that upon lithiation, the initial tetrahedral Zn centers migrate to the open octahedral sites (16c) as the structure

[1]*Energy Science and Photon Sciences Directorate, Brookhaven National Laboratory, Upton, NY 11973*
[2]*Department of Chemistry, State University of New York at Stony Brook, Stony Brook, NY 11794-3400*
[3]*Present Address: Department of Chemistry, Valparaiso University, Valparaiso, IN 46383-6493*
[4]*Department of Materials Science and Chemical Engineering, State University of New York at Stony Brook, Stony Brook, NY 11794-2275*
[5]*Department of Chemistry, Elmira College, Elmira, NY 14901*
[6]*ExCELS Research Experience for Undergraduates, Stony Brook University, Stony Brook, NY 11794-3400*
[7]*Department of Mechanical Engineering, The College of New Jersey, Ewing, NJ 08628*
[8]*Research Experience for Undergraduates: Nanotechnology for Health, Energy and the Environment, Stony Brook University, Stony Brook, NY 11794*
**Corresponding Author Email: kenneth.takeuchi.1@stonybrook.edu*
†equivalent contributions by D.C.B and K.R.T.
Electronic Supplementary Information (ESI) available: EXAFS modelling, operando XRD]. See DOI: 10.1039/x0xx00000x

accommodates the incoming Li^+.[10] The lithiation then proceeds with formation of a rock-salt-like phase where Zn and Fe are in octahedral locations, $Li_2Zn_{[16c]}Fe_{2[16d]}O_{4[32e]}$. Notably, the final discharge products determined in the study were Fe metal and ZnO, while previous reports also observed the presence of Zn metal[11] or a LiZn alloy.[8, 12] There is no consensus in the literature on nature of the re-oxidized reaction products, which have been reported to be ZnO and Fe_2O_3,[11, 12] ZnO and FeO,[13] or coexisting ZnO, LiZn, FeO, and Fe_2O_3.[14]

In contrast to $ZnFe_2O_4$, $MgFe_2O_4$ exists as a partially inverse spinel structure comparable to an inverse spinel; however, the distribution of cations can vary between octahedral and tetrahedral sites.[15] The theoretical capacity of $MgFe_2O_4$ is 804 mAh/g corresponding to 6 electron equivalents, as the very weak oxidizing agent MgO is not reduced to Mg metal during the discharge process.[9, 16] The redox mechanism of $MgFe_2O_4$ was recently investigated using X-ray diffraction, ^{7}Li NMR spectroscopy, and ^{57}Mössbauer spectroscopy.[17] Upon 2 electron equivalents of lithiation, XRD indicated that the $MgFe_2O_4$ electrodes underwent a phase transition from spinel $MgFe_2O_4$ to the rock salt FeO structure. Mossbauer spectroscopy indicated reduction of an additional 4 electron equivalents resulted in Fe^{2+} being fully reduced to metallic Fe^0, which was then subsequently oxidized to Fe^{2+} on charge. While this previous report was able to effectively determine oxidation state of the iron during (de)lithiation, the lack of long range order made it impossible to definitively assess the structural evolution of the material after only 2 electron equivalents of lithiation.

In this study, we present a combined X-ray absorption spectroscopy, X-ray diffraction and density functional theory (DFT) study of the spinel ferrites Fe_3O_4, $MgFe_2O_4$, $ZnFe_2O_4$ to elucidate the role of the +2 cation on the structural evolution and phase transformations occurring during de(lithiation) processes. Collectively, this series of compounds allows retention of the spinel oxide structure, but with different Fe octahedral/tetrahedral site occupancies and different attainable levels of reduction (e.g., Zn^{2+} to Zn^0 but not Mg^{2+} to Mg^0). The three target materials were synthesized to have crystallite sizes between 9 and 13 nm in order to minimize variability in mechanistic behavior that has been shown to occur with materials of large crystallite size differences.[3, 17] X-ray absorption spectroscopy is well suited to investigate the redox mechanisms of these materials, which become nanocrystalline after initial lithiation, as the technique does not rely on a long range periodic structure to obtain meaningful data. Furthermore, by analyzing both X-ray absorption near-edge structure (XANES) and extended X-ray absorption fine structure (EXAFS), we can provide complementary information regarding the local electronic and atomic structure on the same sample. XAS has been used to investigate the structural changes associated with lithiation of spinel ferrites with substituted +2 cations including $ZnFe_2O_4$[10] $CoFe_2O_4$[18, 19], $NiFe_2O_4$[18, 20, 21], and $CoMnFe_2O_4$[19], including in some cases EXAFS modeling as a function of lithiation level.[10, 19, 21] However, this is the first EXAFS-based study that presents comparative EXAFS modeling of iron spinel ferrites with differing +2 cation and degree of inversion under the same electrochemical (dis)charge conditions and with similar crystallite size. This report also includes the first EXAFS modeling investigation of the $MgFe_2O_4$ chemistry. Complementary to the XAS measurements, synchrotron X-ray Diffraction (XRD) and DFT were used to investigate the initial lithiation process (< 2 electron equivalents of reduction), before the materials became too nanocrystalline for diffraction measurements. The study provides evidence for (1) a general Li^+ ion insertion mechanism occurring in the ferrite spinel framework during initial lithiation, (2) the formation of Zn metal in fully discharged $ZnFe_2O_4$, (3) highly amorphous FeO domains resulting from delithiation which have a coordination environment that is distorted from a pure octahedral environment (rock salt structure), and (4) reversible cycling between metal nanoparticles (discharge) and disordered, segregated mono-oxide domains (FeO, MgO, ZnO) during charge.

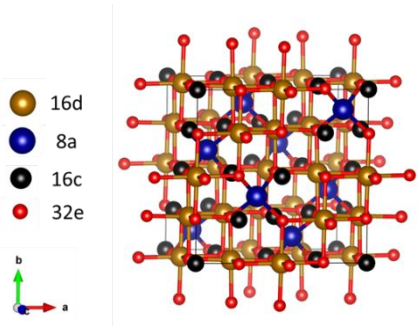

Figure 1. Representative structure of spinel ferrite oxides viewed down the (001) axis. Cations occupy tetrahedral (8a) sites and octahedral (16d) sites, with oxygen atoms at the 32e sites. Octahedral (16c) vacancies in the structure are also indicated.

Experimental Section

Materials Synthesis and Characterization

Magnetite, Fe_3O_4, was synthesized as previously described.[22] Briefly, magnetite was prepared from a coprecipitation reaction using $FeCl_2{\cdot}4H_2O$ and $FeCl_3{\cdot}6H_2O$ precursors. Coprecipitation was also used to synthesize $MgFe_2O_4$ where an aqueous solution of $Mg(NO_3)_2{\bullet}6H_2O$ and $Fe(NO_3)_3{\bullet}9H_2O$ was added dropwise to a sodium hydroxide solution. The precipitate was collected, heated hydrothermally at 140°C for 10 hr. and then annealed in air at 400°C for 2 hours. $ZnFe_2O_4$ was prepared using a coprecipitation method followed by a hydrothermal step.[10] Briefly, an aqueous solution containing $Fe(NO_3)_3{\cdot}9H_2O$ and $Zn(NO_3)_2{\cdot}6H_2O$ was added dropwise into an aqueous triethylamine solution. The precipitate was collected and placed into a hydrothermal vessel at 220 °C for 10 hours.

Quantitative elemental analysis was determined by inductively coupled plasma-optical emission spectroscopy (ICP-OES) using a ThermoScientific iCap 6000 spectrometer. Quantitative elemental composition was determined by inductively coupled plasma-optical emission spectroscopy (ICP-OES) using a ThermoScientific iCap 6000 spectrometer.

Electrochemical Methods

Electrodes were prepared on copper foil substrates with active material, carbon black, and poly vinylidene difluoride binder in a ratio of 80:10:10. The mass loading for the electrodes ranged between 4 – 5 mg/cm^2. Cells in a coin cell configuration were used for electrochemical tests with lithium metal counter

electrodes, polypropylene separators and 1 M lithium hexafluorophosphate ($LiPF_6$) in the solvent mixture 30:70 (v:v) ethylene carbonate:dimethyl carbonate electrolyte. Coin cells were galvanostatically tested at a rate of C/30 to various (de)lithiation and cycled states for further XAS analysis. Specifically, the electrodes were lithiated to 0.5 ee, 1 ee, 2 ee, 4 ee, 6 ee, or 0.05 V and then delithiated to 4 ee or 3.0 V. The fully lithiated and fully delithiated states for cycle 2 were also prepared. Reported capacities were calculated based on the mass of the active material in the electrode.

X-ray Absorption Spectroscopy

Prior to measurement, the samples were prepared and stored under Ar atmosphere to prevent oxidation. XAS spectra were collected at sectors 10-BM and 12-BM at the Advanced Photon Source at Argonne National Laboratory, IL. Measurements were collected at the Fe K-edge (7112 eV) and Zn K-edge (9659 eV) in transmission mode using a Si (111) double crystal monochromator. All samples were measured with a metal foil reference simultaneously for correct energy alignment of individual spectra during data analysis.

XAS spectra were aligned, averaged, and normalized using Athena.[23] The built-in AUTOBK algorithm was used to limit background contributions below R_{bkg} = 1.0 Å. Normalized spectra were fit utilizing Artemis with theoretical structural models created with FEFF6.[23, 24] A k-range of 2 – 10 $Å^{-1}$ and Hanning window (dk = 2) were used as Fourier transform parameters, and fitting was performed in k, k^2 and k^3 k-weights simultaneously. An R-range of 1.0 – 3.7 Å or 1.0 – 3.0 Å was used to fully encompass the first and second shells of |χ(R)| (Fourier transform of χ(k)). Additionally, S_0^2 values were determined from fitting Fe and Zn metal standards, and these terms were applied to all fits to account for intrinsic losses in the electron propagation and scattering processes.

The undischarged spectrum of Fe_3O_4 was fit using inverse-spinel $Fd\overline{3}m$ Fe_3O_4.[25] An $MgFe_2O_4$ structural model was created utilizing the nominal inverse-spinel $Fd\overline{3}m$ Fe_3O_4 crystal structure and replacing 50% of Fe atoms located at the 16d site with Mg in the FEFF calculation. For $ZnFe_2O_4$, a theoretical structural model based on $ZnFe_2O_4$ was used.[26] In addition to the pristine structures, modified $Fd\overline{3}m$ structures with cations in 16c sites, body centered cubic (bcc) Fe metal[27], and hexagonal close packed (hcp) Zn metal[28] structural models were also utilized to model the various (dis)charged phases. The results of the EXAFS fits were used to determine the phases at each electrochemical state. If a specific phase resulted in low relative amplitude (near 0 with estimated standard deviations) or fitting variables were statistically insignificant, the phase was excluded from the model.

Synchrotron X-ray Diffraction

X-ray diffraction patterns of the pristine materials were collected at the 28-ID beamline at the National Synchrotron Light Source II (NSLS-II) at Brookhaven National Laboratory, NY. For pristine samples of Fe_3O_4, $ZnFe_2O_4$, and $MgFe_2O_4$, the x-ray wavelength was calibrated to 0.18990 Å, 0.23699 Å and 0.23720 Å, respectively. Operando XRD was collected using custom-built cells. Ferrite and Li metal electrodes were used and discharged at a 50 mA/g rate to a limit of 2 electron equivalents. Operando scans were collected at 8 minute intervals yielding ~32 measurements for each ferrite material (Fe_3O_4, $MgFe_2O_4$, and $ZnFe_2O_4$). A 16-inch CsI scintillation detector was used to collect the data. LaB_6 was used as a standard. Each two-dimensional pattern was integrated and data were analyzed using GSAS-II.[29] The synchrotron XRD data was refined using a nominal Uiso value of 0.01 $Å^2$ and microstrain of 0.1%. For refinement of pristine materials, the Mg:Fe and Zn:Fe ratios were constrained to 1:2, based on the elemental ratios determined from ICP-OES.

DFT Calculations

DFT implemented in the Vienna ab initio simulation package (VASP)[30, 31] was employed to describe the initial lithiation behaviors of AFe_2O_4 (A=Zn, Mg). The spin-polarized DFT+U calculations[32, 33] were carried out using the Projector Augmented-wave (PAW) potential[34, 35] and the Perdew-Burke-Ernzerhof (PBE) exchange-correlation functional[36] with a kinetic energy cutoff of 520 eV. A Hubbard U correction of U_{eff} = 5.3 eV was applied to describe the Fe d orbitals, according to our previous studies of AFe_2O_4 bulks and surfaces. [10, 37-39] The Gaussian smearing method was used with the total energies converged better than 10^{-4} eV, and the final force on each atom is less than 0.02 eV $Å^{-1}$. The first Brillouin zone was sampled on 4 × 4 × 4 Γ-centered grid. Such setup, including the applied U value, was successfully used to predict the lattice constants and the lithiation properties for AFe_2O_4 observed experimentally.[10, 37-39] The corresponding formation energies for $Li_xAFe_2O_4$ (A=Zn, Mg) were calculated as

$$\mathbf{E_f} = \frac{\mathbf{E(Li_xAFe_2O_4) - E(AFe_2O_4) - xE(Li)}}{\mathbf{x}} \quad (1)$$

according to the previous study,[40] where E is the DFT calculated total energy of a specific configuration. "x" is the lithiation (discharge) extent. E(Li) is constant and is equal to the total energy of bulk metallic Li, which is assumed as the anode. E_f was expressed in eV per formula unit. The structure with a lower formation energy is more preferable.

Results and Discussion

Synthesis and Characterization

Fe_3O_4 was synthesized via coprecipitation[22], while $ZnFe_2O_4$ was prepared using coprecipitation and subsequent hydrothermal treatment.[10] Magnesium ferrite ($MgFe_2O_4$) was prepared by a combination of co-precipitation and hydrothermal reactions with a subsequent calcination step modified from previously reported syntheses.[41, 42] Synchrotron XPD was used to characterize the structure of the synthesized materials. Rietveld refinement results of the pristine materials are shown in **Figure S1** and tabulated **in Table S1**. All three materials adopt the *Fd$\overline{3}$m* space group for cubic spinels, with crystallite sizes between 10 and 13 nm. Fitting results indicate that for $ZnFe_2O_4$,

100% of Zn ions are located in the 8a site, with the 16d site occupied by Fe ions. For the $MgFe_2O_4$ sample, a two phase fitting model was used to fit the data. Both phases consist of $MgFe_2O_4$, but with significantly different crystallite sizes (15.2 nm and 2.7 nm). Refinement of fractional occupancy indicates that both phases adopt a partially inverse spinel structure.

ICP-OES was used to verify the elemental composition of the $ZnFe_2O_4$ and $MgFe_2O_4$ samples. Elemental analysis from ICP-OES showed a Zn/Fe ratio of 1.02:2 for $ZnFe_2O_4$ and a Mg/Fe ratio of 1.00:2 for $MgFe_2O_4$, consistent with the expected stoichiometry.

Electrochemistry

Coin type half cells were prepared with lithium counter electrodes and working electrodes consisting of the three spinel ferrites under study. The three groups of cells were galvanostatically cycled at a C/30 rate between 3.0 V and 0.05 V vs. Li/Li^+. Representative voltage profiles for the first and second (de)lithiation cycles are plotted vs. number of electron equivalents in **Figure 2.** The theoretical number of electrons discharged for Fe_3O_4 and $ZnFe_2O_4$ is eight, corresponding to full electrochemical reduction of Fe and Zn atoms to Fe^0 and Zn^0. (Equations 2 and 3). $MgFe_2O_4$ is anticipated to only deliver 6 electron equivalents upon full lithiation due to the electrochemical inactivity of formed MgO[16, 17] (Equation 4).

$$Fe_3O_4 + 8\ Li^+ + 8\ e^- \rightarrow 3\ Fe^0 + 4\ Li_2O \quad (2)$$

$$ZnFe_2O_4 + 8\ Li^+ + 8\ e^- \rightarrow Zn^0 + 2\ Fe^0 + 4\ Li_2O \quad (3)$$

$$MgFe_2O_4 + 6\ Li^+ + 6\ e^- \rightarrow MgO + 2\ Fe^0 + 3\ Li_2O \quad (4)$$

In the case of each of the three materials, the discharge capacity delivered during the first cycle is greater than the theoretical prediction. The high first discharge capacities are irreversible and are associated with solid electrolyte interphase (SEI) formation on the electrodes.[43-46] Prior reports have investigated the chemical composition of the SEI on spinel ferrites,[44, 47] and the parasitic heat associated with the electrolyte deposition has been quantified by isothermal microcalorimetry.[44, 45] Differences in the voltage profiles among the materials are observed. For Fe_3O_4 and $ZnFe_2O_4$, short voltage plateaus are observed between *ca.* 1.6 V and 1.4 V, and again at ~1.2 V. The first plateau has been reported to be associated with initial insertion of a Li^+ ion into the interstitial octahedral sites of the inverse spinel structure, while the second plateau originates from the shifting of tetrahedral Fe ions in Fe_3O_4 and tetrahedral Zn ions in $ZnFe_2O_4$ to octahedral sites during continued lithiation.[4, 12] In contrast, for $MgFe_2O_4$, the voltage plateaus in these regions are less pronounced and have greater slope. At ~0.8 V, both Fe_3O_4 and $ZnFe_2O_4$ exhibit a long voltage plateau which is attributed to the conversion reaction. The $MgFe_2O_4$ voltage profile is more sloping suggesting the occurrence of additional electrochemical reactions.

Upon delithiation to 3.0 V, all three materials exhibit a sloping voltage curve with higher average voltage than the preceding lithiation process. Fe_3O_4 and $ZnFe_2O_4$ deliver a delithiation capacity equivalent to ~8 electrons, while that of $MgFe_2O_4$ is 5.8 electron equivalents. During the second lithiation, delivered capacities are lower than during cycle 1, at 8.8 ee, 8.2 ee, and 5.6 ee for Fe_3O_4, $ZnFe_2O_4$, and $MgFe_2O_4$, respectively. The large irreversible capacity observed between cycle 1 and cycle 2 is attributed to SEI formation on the electrodes during the first discharge.[43-46]

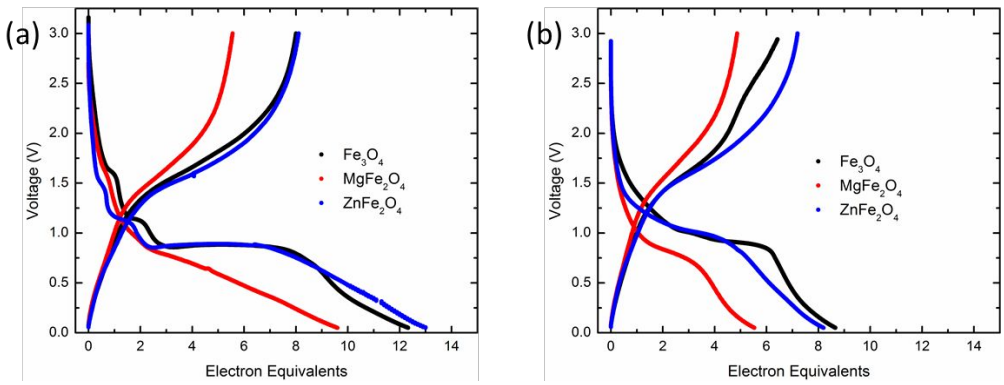

Figure 2. Representative voltage vs. electron equivalent profiles for (a) the first cycle and (b) the second cycle of Fe_3O_4, $MgFe_2O_4$, and $ZnFe_2O_4$ electrodes lithiated and delithiated at a C/30 rate in the voltage range 0.05 – 3.0 V.

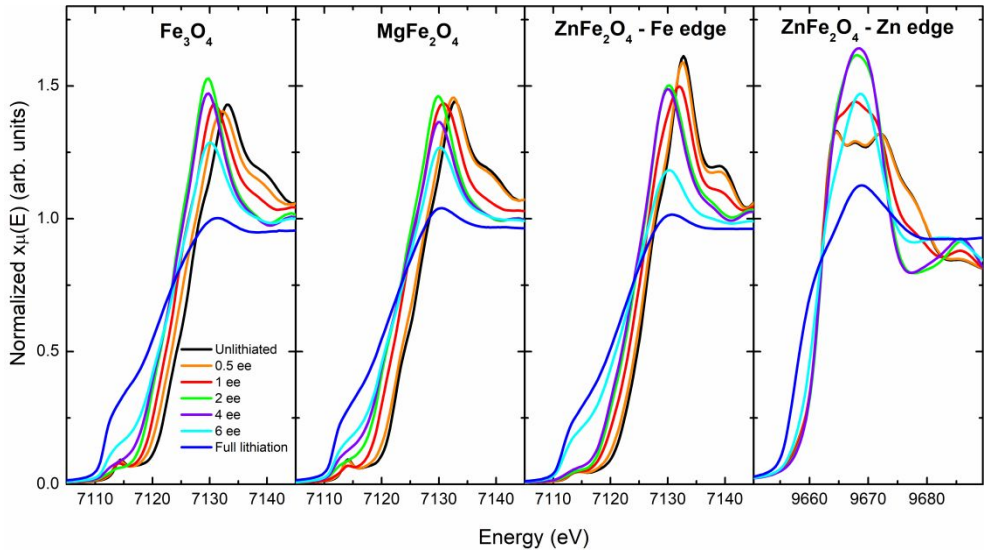

Figure 3. XANES of Fe_3O_4, $MgFe_2O_4$, and $ZnFe_2O_4$ (Fe and Zn K-edges) during first cycle lithiation.

The electrochemistry of the three materials was characterized using cyclic voltammetry (**Figure S2**). During the first reduction sweep, three cathodic peaks are observed for Fe_3O_4 and $ZnFe_2O_4$ electrodes at potentials of approximately 1.55, 1.05, and 0.65 volts, corresponding with the potential plateaus observed during the first galvanostatic discharge (**Figure 2**) and in good agreement with prior reports.[10, 48] These three peaks correspond to (1) initial Li^+ insertion in the spinel structure, (2) phase transformation from spinel to rock-salt like structure, and (3) conversion to the final discharge products along with formation, respectively.[48] In the $MgFe_2O_4$ electrode, the first and second reduction peaks are not well resolved, in agreement with the lack of well defined plateaus at ~1.55 V and ~1.05 V observed in the first cycle voltage profile. The relative areas under the CV curves agree well with the delivered capacities observed via galvanostatic cycling. The first anodic sweep for all three materials has a broad peak in the range of 1.6–1.8 V which characterize the discharge product conversion to the charge products. Cycle 2 and 3 CV profiles show a primary cathodic peak which is shifted higher to 0.65–0.9 V, in agreement with the reduced polarization observed in the cycle 2 galvanostatic discharge profiles, and anodic peaks at 1.6–1.8 V.

X-ray Absorption Spectroscopy – XANES

Ex-situ X-ray absorption spectroscopy (XAS) was used to probe the redox mechanisms of Fe_3O_4, $MgFe_2O_4$, and $ZnFe_2O_4$ at various states of (de)lithiation. XAS is a powerful technique for studying these materials as it does not rely on a long range periodic structure to obtain meaningful data.[49] Specifically, the X-ray absorption near-edge structure (XANES) and extended X-ray absorption fine structure (EXAFS) regions of XAS spectra provide valuable insight into local electronic and atomic environment, respectively. In this study, the information extracted from XANES and EXAFS are used complementary to each other to deliver a detailed mechanistic view of the electrochemical (de)lithiation processes of the spinel ferrite materials under study during the first two cycles. **Figure 3** shows the XANES spectra of Fe_3O_4, $MgFe_2O_4$, and $ZnFe_2O_4$ electrodes during the first cycle lithiation process (0.5 ee, 1 ee, 2 ee, 4 ee,

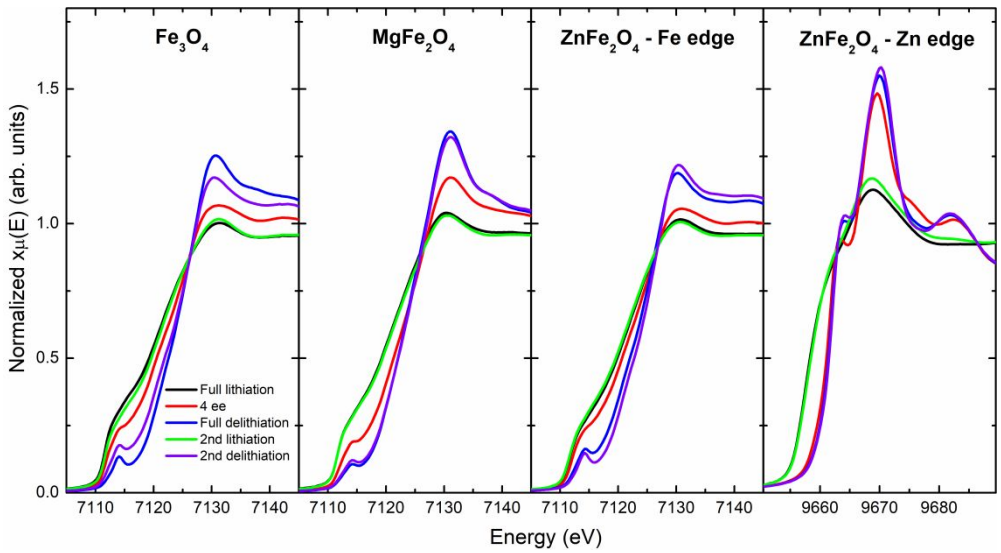

Figure 4. XANES of Fe_3O_4, $MgFe_2O_4$, and $ZnFe_2O_4$ (Fe and Zn K-edges) during first and second cycle (de)lithiation.

6 ee, and fully lithiated states), while **Figure 4** shows XANES spectra in the cycle 1 fully lithiated, 4 ee delithiated and fully delithiated states, as well as cycle 2 fully (de)lithiated states.

In the pristine state, the edge energy (defined as the maximum of the first derivative of μ(E)) of the Fe_3O_4 electrode has a value of 7126.6 eV, in good agreement with previous reports.[3] As the material is lithiated, the edge energy gradually shifts to lower values, consistent with the electrochemical reduction of Fe. Furthermore, the intensity of the pre-edge peak present at ~7114.5 eV in the pristine material significantly decreases between the pristine and 2 ee lithiated states. In the pristine material, Fe atoms are located in the tetrahedral 8a site with non-centrosymmetric symmetry – that is, lacking an inversion center – and T_d point group, for which $p_{x,y,z}$ and $d_{xy,\ xz,\ yz}$ orbitals both belong to the irreducible representation T_2; thus hybridization of 3d and 4p orbitals occurs.[50] The electric dipole transition of 1s electrons to the p-component of these d-p hybridized orbitals results in high pre-edge peak intensity observed for the pristine material.[50-52] The reduction in pre-edge peak intensity with lithiation suggests that Fe atoms are shifting from tetrahedral to octahedral sites (O_h point group), where there are no irreducible representations for which both d- and p orbitals belong. Migration of Fe from tetrahedral to octahedral sites during initial lithiation of Fe_3O_4 has previously been observed experimentally[2] and was predicted by DFT calculations.[4] The edge energy decreases to 7123.7 eV by 4 ee and 7112 eV upon full lithiation, signifying that the primary oxidation state of the reduced material is Fe^0. Remnant lower pre-edge intensity is observed beyond 2 electron equivalents of reduction, when Fe is anticipated to exist in octahedral coordination environments. The remnant observed intensity is ascribed to electric dipole transitions to p-d hybrid orbitals from Fe-O hybridization, rather than to electric quadrupole transitions, which are theoretically calculated to be 2 orders of magnitude weaker in intensity.[52-54]

During subsequent delithiation to 4 ee, the edge position and profile of the XANES spectra indicate that Fe atoms in the electrode are mixture of metallic and oxidized phases. The fully delithiated electrode (charged to 3.0 V) has an edge energy of 7125.3 eV, which is ~1.3 eV lower than the pristine electrode, indicating that the material does not fully re-oxidize to Fe_3O_4. The fully delithiated state has a significantly reduced white line intensity (at *ca.* 7132 eV) compared to the pristine electrode, signifying that the Fe atoms have a different electronic structure. Notably, the pre-edge peak re-emerges in the delithiated state. This finding suggests that a portion of the re-oxidized Fe-atoms are in a non-centrosymmetric coordination environment allowing for p-d hybridization, leading to intense pre-edge intensity arising from electric dipole transitions. In the second cycle, a metallic Fe edge position of 7112 eV is reached on full lithiation, while the delithiated state has edge position of 7125.1 eV, slightly lower than cycle 1 and indicative of the lower oxidation state in the second cycle.

The progression of XANES spectra during (de)lithiation for the $MgFe_2O_4$ electrode is reminiscent to that of Fe_3O_4. The initial edge energy of the $MgFe_2O_4$ electrode is slightly higher than Fe_3O_4 (7126.8 eV for $MgFe_2O_4$, 7126.6 for Fe_3O_4) due to the higher average Fe oxidation state (+3 for $MgFe_2O_4$ vs +2.67 for Fe_3O_4). A significant pre-edge peak at ~7114.5 eV is also observed, indicating that a significant fraction of the Fe atoms are in tetrahedral sites, in agreement with the XPD refinement results, that enable a dipole transition to p-d hybridized orbitals.[50, 55-57] During lithiation, the edge energy decreases to 7112 eV upon full lithiation, indicating the presence of Fe metal. The pre-edge peak is reduced in intensity by 2 ee lithiation, suggesting that Fe atoms migrate from tetrahedral to octahedral positions in the spinel structure. On delithiation, the edge position shifts back to ~7124.9 eV, approximately 2 eV lower than that of the pristine material, indicating incomplete reoxidation to Fe^{3+}. As with Fe_3O_4, there is an observable pre-edge feature at ~7114 eV for the charged electrode, indicating that some of the oxidized Fe atoms have a non-centrosymmetric coordination environment without centrosymmetric symmetry. The second cycle edge positions in fully lithiated and delithiated states are similar to those of cycle 1.

XANES spectra of $ZnFe_2O_4$ were collected at both Fe and Zn K-edges to determine the relative oxidation state progression of the two metal centers. In the pristine state, the Fe edge energy is 7126.3 eV, however, the pre-edge feature is significantly

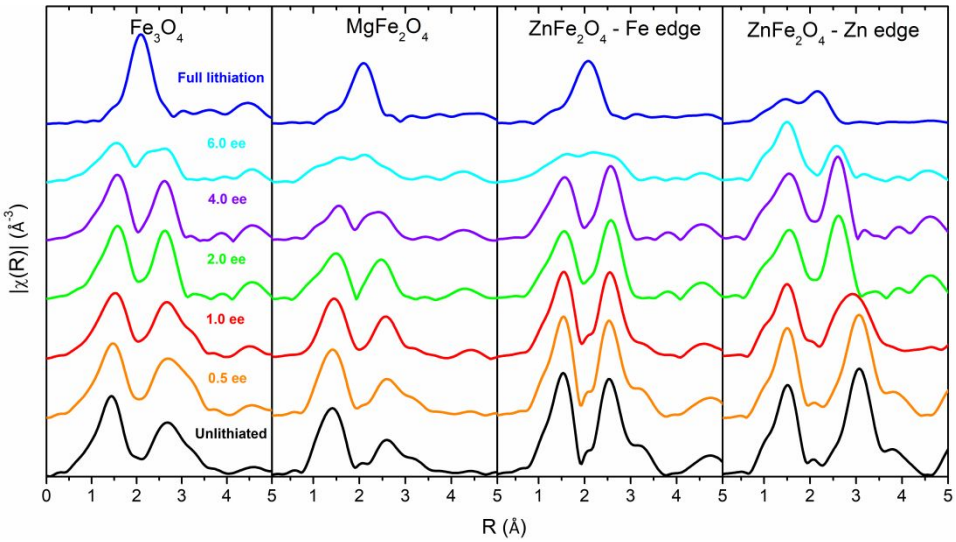

Figure 5. k^2-weighted |χ(R)| of the 1st lithiation process of Fe_3O_4, $MgFe_2O_4$, and $ZnFe_2O_4$ (Fe and Zn K-edges).

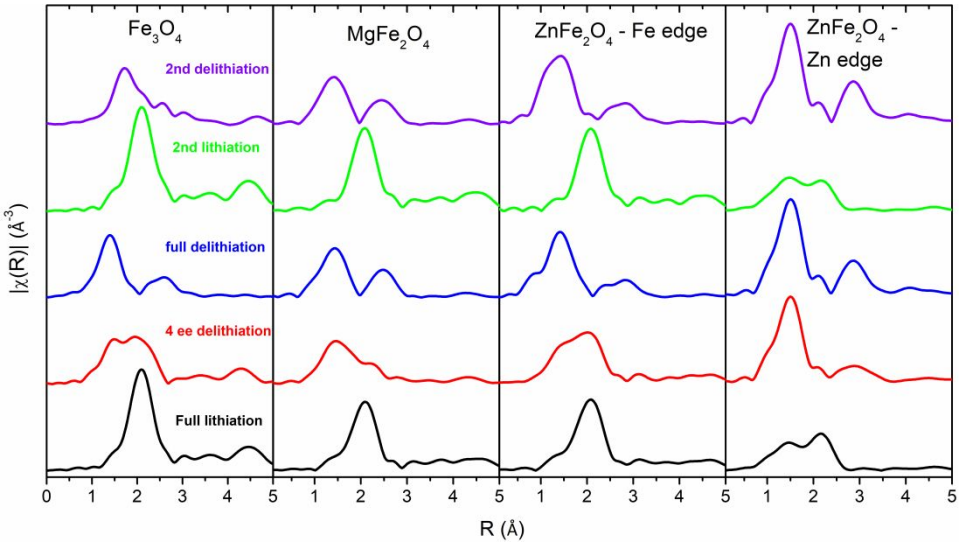

Figure 6. k^2-weighted $|\chi(R)|$ of Fe_3O_4, $MgFe_2O_4$, and $ZnFe_2O_4$ (Fe and Zn K-edges) during first and second cycle (de)lithiation.

reduced in intensity relative to the other two materials. $ZnFe_2O_4$ is a normal spinel, in which Zn^{2+} occupies tetrahedral (8a) sites and Fe^{3+} occupies octahedral (16c) sites. In contrast, Fe_3O_4 is an inverse spinel (Fe^{2+} in octahedral sites, Fe^{3+} in both tetrahedral and octahedral sites) and $MgFe_2O_4$ is a partially inverse spinel with a significant fraction of Fe ions in tetrahedral sites. Unlike Fe_3O_4 and $MgFe_2O_4$, $ZnFe_2O_4$ does not contain tetrahedral Fe and thus electric dipole transitions do not occur, manifesting as lower pre-edge peak intensity.[50] As the $ZnFe_2O_4$ electrode is discharged, the Fe K-edge shifts to a lower energy, reaching 7124.2 eV by 4 ee discharge. The fully lithiated electrode reaches the metallic edge position of 7112. It is notable that in the delithiated state, the XANES spectra are similar in edge position and profile to that of delithiated Fe_3O_4 and $MgFe_2O_4$, suggesting that the re-oxidized Fe atoms in each case have a comparable oxidation state and electronic structure.

In contrast to the Fe K-edge, the Zn K-edge XANES shows significantly less edge shift, moving from a pristine value of 9662 eV to 9658 eV for the fully lithiated material. Although in the pristine electrode Zn^{2+} has T_d symmetry, the 3d band is completely filled and thus the pre-edge peak associated with 1s to 3d transitions is not observable. Notably, the edge position in the fully lithiated state (9657.9 eV) has a lower value than Zn metal (9659), possibly signifying a coordination environment that is different from bulk Zn metal. The formation of LiZn alloy has been suggested previously in fully reduced $ZnFe_2O_4$ electrodes characterized by selected area electron diffraction (SAED) and X-ray photoelectron spectroscopy (XPS),[8, 12, 14] but has not been definitively detected.[11] Upon (de)lithiation, the XANES spectra return to an edge position of ~9662 eV, suggesting that Zn has re-oxidized to +2. The spectra of the cycle 2 fully lithiated and delithiated samples are comparable to the cycle 1 samples.

X-ray Absorption Spectroscopy – EXAFS

The extended X-ray absorption fine structure (EXAFS) region of the XAS spectra were analyzed to determine changes in local atomic structure as a function of (de)lithiation. Results are presented in **Figures 5** and **6** as R-space plots (Fourier transforms of $k^2|\chi(k)|$). Note that distances shown in the R-space plot are not corrected for phase shifts and thus are 0.3 – 0.4 Å less than the true interatomic distances from EXAFS modeling results.

Examination of the EXAFS spectra for the pristine Fe_3O_4 sample shows two primary coordination shells centered at 1.4 Å and at 2.6 Å in the $|\chi(R)|$ plots. The first shell at 1.4 Å arises from the back-scattering of nearest neighboring oxygen atoms to both tetrahedrally coordinated (8a site) and octahedrally coordinated (16d site) Fe ions in the inverse spinel structure, while the second coordination shell originates from contributions from nearest neighbor Fe atoms and second shell oxygen atoms. As the material is discharged, evolution of the spectra occurs such that these initial peaks decrease in intensity simultaneous to the growth of a single peak centered at approximately 2.1 Å, indicative of Fe metal. During the subsequent charge, the spectra do not return to that of the undischarged state, signifying significant variation in the recharged phase. Similar changes are observed during the second cycle.

To provide quantitative insight into the observed spectral evolution, the EXAFS were modeled using Artemis software.[23] **Figures 7** and **8** show interatomic distances and relative amplitudes, respectively, for selected coordination paths. Relative amplitudes are defined as the scaled number of near neighbors in each phase, with bulk material having a theoretical relative amplitude of 1. Full fitting parameters (R-factors, E_0 and Debye-Waller factors, interatomic distances, and near neighbors for all 48 spectral fits) are presented in the supplemental information file, **Tables S2 – S12**. The undischarged Fe_3O_4 material was fit using a theoretical model of the inverse spinel Fe_3O_4 structure[25] with 1/3 of Fe atoms located in tetrahedrally coordinated 8a sites and 2/3 of the Fe atoms residing in octahedrally coordinated 16d sites. The reported relative amplitude of the starting phase is only 0.875 ± 0.125, indicative of the small Fe_3O_4 particle size which results in lower observed coordination number.[3] During initial reduction through 1ee, minimal changes were observed in the either the number of interatomic distances or the coordination numbers, indicating that the original Fe_3O_4 structure was maintained. However, by 2 ee a significant reduction in the

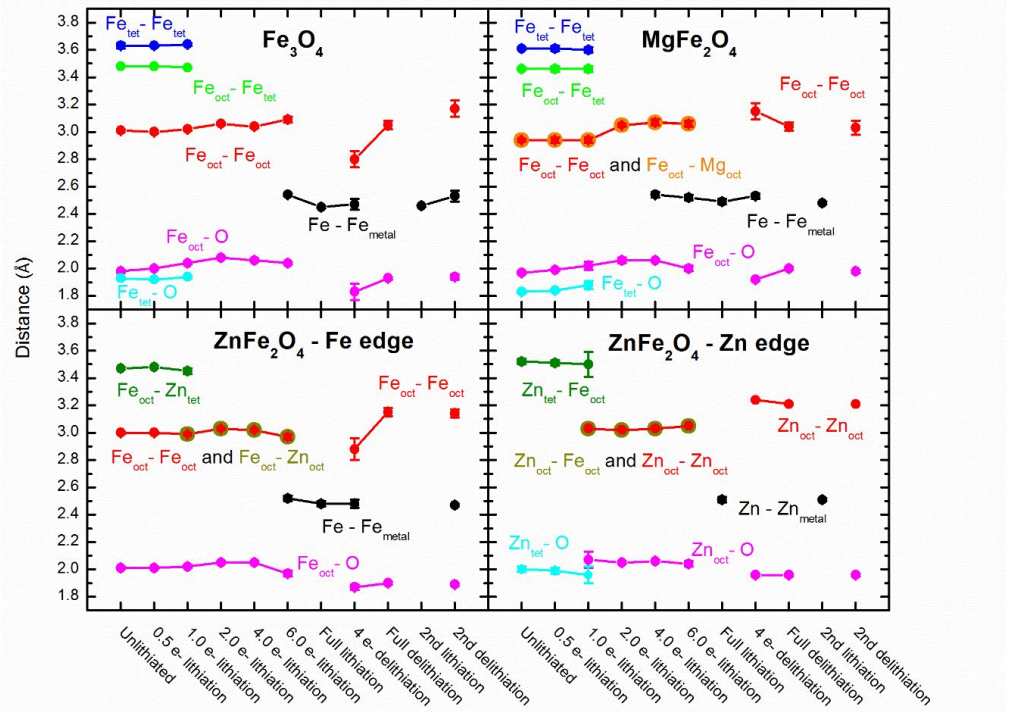

Figure 7. Selected interatomic distances determined from EXAFS fits of Fe_3O_4, $MgFe_2O_4$, and $ZnFe_2O_4$ (Fe and Zn K-edges) at various stages of (de)lithiation. All fitting results are presented in full in the Supplemental Information. Error bars are included in the plots but are in some instances smaller than the symbols for the reported interatomic distances.

intensity of the shoulder in the second coordination shell is detected. Since the shoulder peak arises from Fe atoms in the tetrahedral (8a) environment (Fe_{tet}-Fe_{tet} distance of 3.63± 0.02, Fe_{tet}-Fe_{oct} distance of 3.48 ± 0.02; Fe_{tet}-O distance of 3.61 ± 0.08 Å in the undischarged electrode), the loss of intensity indicates a significant reduction in Fe atoms located in the 8a site. The best fit to the spectra (combined R-factor of 1.2) was obtained by using a modified structure where Fe atoms are located in both 16d sites and previously vacant 16c sites, with the 8a sites no longer occupied. In this rock-salt like phase, Fe atoms in the 16c and 16d sites were modeled as having equivalent Fe-Fe interatomic distance of 3.06 ± 0.01 Å and equivalent Fe-O distances of 2.08 ± 0.1 Å and 3.73 ± 0.04 Å for the first and second coordination shells, respectively. The shift of Fe atoms of 8a to 16c sites below 2.0 electron equivalents of reduction is predicted by DFT+U calculations and is caused by strong electrostatic repulsion between the Fe_{8a} ions and Li ions intercalated into interstitial 16c sites during the initial lithiation steps.[4] This repulsive force displaces the Fe_{8a} ions into neighboring 16c sites, with Li ions redistributing between tetrahedral sites 8a, 8b, and 48f.[4] In particular, high-angle annular dark field imaging of Fe_3O_4 discharged to 2 electron equivalents provides clear experimental evidence of Li located in 8a, 48f, and 8b sites in the spinel framework.[4] The relative amplitude of the $Li_2[Fe_3]_{16c/16d}O_4$ phase is 0.78 ± 0.07 Å, based on theoretical coordination numbers of 6 and 12 for Fe-O and Fe-Fe paths, respectively.

Upon further lithiation to 4 ee, the relative amplitude of the $Li_2[Fe_3]_{16c/16d}O_4$ phase has decreased to 0.63 ± 0.03. The significant reduction in amplitude of the $Li_2[Fe_3]_{16c/16d}O_4$ phase suggests that some amount of conversion to Fe^0 and Li_2O has begun to occur. By 6 ee, the formation of Fe^0 is evident, with characteristic Fe-Fe paths at 2.54 ± 0.02 Å and 2.93 ± 0.02 Å. In the fully lithiated electrode, all Fe atoms have completely converted to Fe^0, with the $Li_2[Fe_3]_{16c/16d}O_4$ phase absent from the spectrum. The particle size of the formed Fe^0 was estimated at ~1.4 nm, based on the fitted values from the first coordination shell and assuming spherical shape and bcc structure.[58] This estimate is in good agreement with previous determinations of Fe^0 particle size in fully lithiated Fe_3O_4 electrodes by EXAFS[3] and HRTEM.[4]

Full delithiation of the material results in Fe-O and Fe-Fe interatomic distances of 1.93 ± 0.01 and 3.05 ± 0.03 Å. This Fe-O interatomic distance is approximately 0.1 Å less than that of the $Li_2[Fe_3]_{16c/16d}O_4$ phase during discharge. At the same time, the number of near neighbors for Fe-O and Fe-Fe paths are only 2.4 ± 0.2 and 1.9 ± 0.3, respectively, compared to theoretical values of 6 and 21 for the rock salt FeO structure. Additionally, a second Fe-O path at 3.21 ± 0.05 Å is necessary to account for residual signal in the second coordination shell. These data indicate that the delithiated phase is (1) significantly nanocrystalline, with high ratios of surface to bulk neighboring atoms, and (2) disordered compared to the rock-salt like phase observed during the initial lithiation process. High disorder of the delithiated phase is further supported the significant pre-edge peak in the XANES spectra, which indicates that the Fe-atoms are in a coordination environment with low inversion symmetry, rather than a purely octahedral environment as in rock-salt FeO. Nanocrystallinity of the re-oxidized Fe phase has been observed previously for Fe_3O_4[3, 44], as well as the spinel ferrites $CoFe_2O_4$ and $NiFe_2O_4$.[18]

On the second lithiation of the Fe_3O_4 electrode, the local atomic structure derived from the EXAFS spectra is that of Fe^0, nearly equivalent to that of the fully discharged cycle 1 electrode. However, the second delithiation sample contains an observable amount of Fe^0 metal consistent with the electrochemistry.

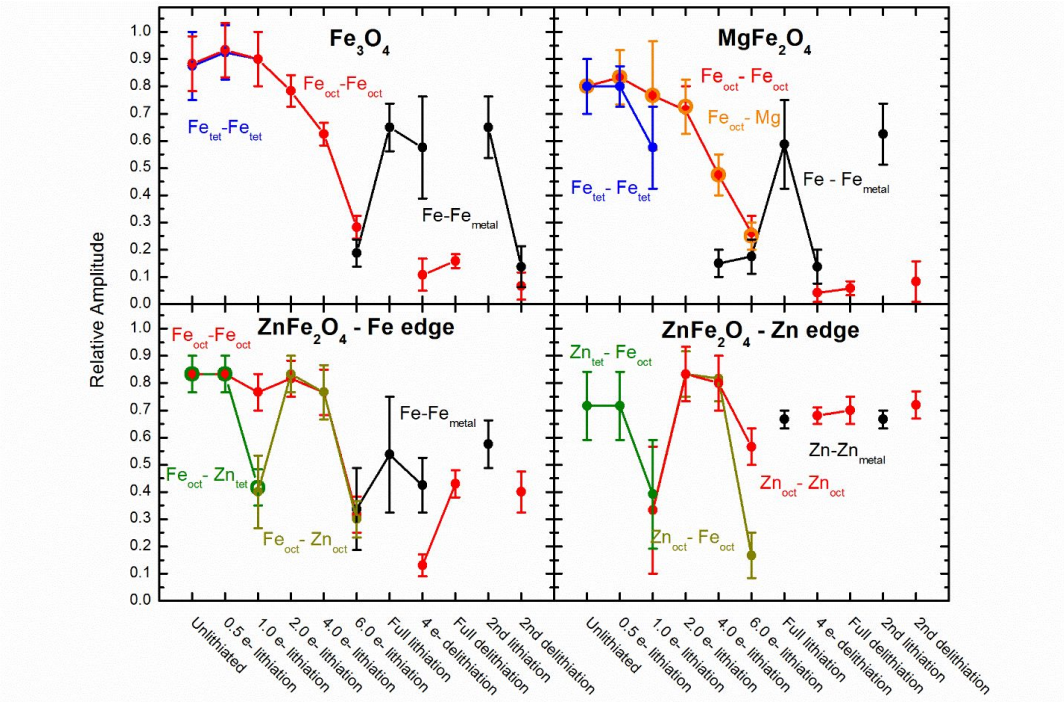

Figure 8. Selected relative amplitudes determined from EXAFS fits of Fe_3O_4, $MgFe_2O_4$, and $ZnFe_2O_4$ (Fe and Zn K-edges) at various stages of (de)lithiation.

The EXAFS spectra of undischarged $MgFe_2O_4$ are similar to those of Fe_3O_4, with first and second coordination shells centered at 1.4 Å and at 2.6 Å, respectively (**Figure 5**). The undischarged state was modelled with all Mg atoms and 1/2 of Fe atoms sharing 16d sites in the inverse spinel structure, with the remaining ½ of Fe atoms located in the 8a positions. The nearly equivalent pre-edge peak intensities between undischarged Fe_3O_4 and $MgFe_2O_4$ suggest that a high proportion of Fe atoms are located in the non-centrosymmetric tetrahedral 8a site in the $MgFe_2O_4$ structure. Although a fraction of Mg atoms may be present in the 8a site, this model was selected to limit the number of fitting variables and enable fits with high statistical significance. Similar interatomic distances are observed between the undischarged Fe_3O_4 and $MgFe_2O_4$ spectra, with the primary variation consisting of contracted Fe_{oct}-Fe_{oct} and Fe_{tet}-O distances in the $MgFe_2O_4$ structure. The relative amplitudes of the two starting phases are within statistical error of each other. As with Fe_3O_4, no substantial structural variation is observed at the 0.5 ee discharge level. Between 0.5 ee and 1 ee, there is a decrease in the number of Fe_{tet}-Fe_{tet} near neighbors (from 1.1 ± 0.1 to 0.8 ± 0.1) and by 2 ee, no statistically significant Fe_{tet} paths can be modeled. Instead, the structural model producing the best fit (combined R-factor = 2.0) is that in which all Fe_{tet} ions have migrated to the 16c site, and thus all Mg and Fe atoms are in octahedral coordination environments. This $Li_2[Mg]_{16d}[Fe_2]_{16c/16d}O_4$ model is analogous to the rock-salt like structure which produced the best fit for the Fe_3O_4 electrode at 2 ee. A *ca.* 0.1 Å increase in the Fe_{oct}-Fe_{oct} and Fe_{oct}-Mg_{oct} interatomic distances is also observed at 2 ee such that these distances are now within statistical error of the Fe_{oct}-Fe_{oct} path in the 2 ee Fe_3O_4 electrode.

Continued lithiation of the electrode results in the appearance of Fe^0 at 4 ee, with a corresponding decrease in relative amplitude of the $Li_2[Mg]_{16d}[Fe_2]_{16c/16d}O_4$ phase. It is notable that Fe^0 can be modeled at 4 ee in the $MgFe_2O_4$ electrode, compared to the Fe_3O_4 electrode, where it is not observed until $6e^-$. At 4 ee, the theoretical percentage of Fe atoms in $MgFe_2O_4$ that are converted to Fe^0 is ~50% while in Fe_3O_4 this percentage is only 33%. Because of the higher percentage of Fe converted to metal at 4 ee in $MgFe_2O_4$, the Fe^0 EXAFS signal is more readily detected. At 6 ee, the relative amplitudes of paths associated with Fe_{oct} drop to 0.27 ± 0.7, and in the fully lithiated state only the contributions from the Fe^0 phase are observed. The estimated size of the Fe^0 particles from the first shell fitted coordination number[58] is ~0.9 nm.

The local atomic structure of the delithiated $MgFe_2O_4$ electrode is similar to that of delithiated Fe_3O_4, with (1) reduced first shell Fe-O interatomic distance compared to the $Li_2[Mg]_{16d}[Fe_2]_{16c/16d}O_4$ phase during lithiation, (2) low relative amplitudes for all nearest neighboring atoms, and (3) a second Fe-O path above 3 Å. These findings suggest that the re-oxidized phase is a highly disordered iron oxide. It is also notable that no statistically significant Fe-Mg paths can be modeled, indicating phase segregation between FeO and MgO domains in the charged state. In a previous report it was claimed that FeO is the reformed product[17], but this was only speculation since scattering domains of the recharged product were too small to be detected by X-ray diffraction.

At the Fe K-edge, the first and second coordination shells of the pristine $ZnFe_2O_4$ electrode are centered at *ca.* 1.4 Å and 2.5 Å, respectively, while at the Zn K-edge, the second coordination shell is shifted to ~3.0 Å. The pristine state was modeled using the nominal structure for $ZnFe_2O_4$[26], with all Zn atoms occupying the tetrahedral 8a sites and all Fe atoms occupying the octahedral 16d sites. This model accounts for the shift of the second coordination shell at the Zn edge, which is caused by the absence of Zn_{oct}-Zn_{oct} scattering paths. Good correlation in the fitting parameters was obtained for the modeling results at the

two absorption edges, with the Fe_{oct}-Zn_{tet} path determined to have an interatomic distance of 3.47 ± 0.01 Å and 3.50 ± 0.02 Å for the Fe and Zn EXAFS, respectfully. At the 0.5 ee lithiation level, no changes in either the interatomic distances or number of neighboring atoms were observed for any of modeled scattering paths, suggesting that initial lithiation occurs without significant lattice expansion or migration of Fe/Zn ions in the spinel structure. However, by 1 ee there are significant changes in the spectra, most notably a reduction in the shoulder peak at ~3.3 Å at the Fe edge and the beginning of a contraction in the second shell coordination distance at the Zn edge. Fits with high statistical significance were obtained using a second Fe-Zn path at ~3.0 Å. In accordance with a recently published study on (de)lithiated $ZnFe_2O_4$,[10] this path is representative of Zn atoms which have migrated from their initial 8a position to previously unoccupied 16c sites. This is the same general mechanism that we observe for Fe_3O_4 and $MgFe_2O_4$, where 8a cations migrate to 16c sites to form $Li_x[Fe_3]_{16c/16d}O_4$ and $Li_2[Mg]_{16d}[Fe_2]_{16c/16d}O_4$, respectively. The resulting $Li_2[Zn]_{16c}[Fe_2]_{16d}O_4$ structure has Fe-Fe, Fe-Zn, and Zn-Zn paths all 3.02 – 3.03 Å, with a relative amplitude of 0.83 ± 0.08 based on approximately 5 M-M nearest neighbors. Good agreement is observed for fits at the Fe and Zn edge.

The paths associated with the $Li_2[Zn]_{16c}[Fe_2]_{16d}O_4$ structure are maintained at 4 ee of reduction, decreasing only slightly in amplitude. At 6 ee the relative amplitude of Fe-Zn and Fe-Fe paths drop to 0.2 – 0.3, while the Zn-Zn path decreases only slightly to 0.57 ± 0.07 and Fe^0 is observed in the Fe EXAFS. This result suggests that that Fe^{2+} ions in $Li_2[Zn]_{16c}[Fe_2]_{16d}O_4$ are converted to Fe^0 prior to the conversion of Zn^{2+} to Zn^0.

In the fully discharged state, Fe edge EXAFS data indicates complete conversion of Fe ions to Fe^0, with only Fe-Fe_{metal} contributions to the spectra observed. At the Zn edge, the EXAFS data shows contributions from both a Zn-O path at 1.92 ± 0.02 Å and one Zn-Zn_{metal} path at 2.51 ± 0.02 Å. Notably, this data provides the first conclusive evidence of Zn metal formation in lithiated $ZnFe_2O_4$ by XAS. In a previous report only the ZnO phase was observed at the end of discharge, likely due a voltage cutoff of 0.2 V, whereas in this study a voltage cutoff of 0.01 V was utilized.[10] In second previous report, it was proposed that Zn metal is formed along with ZnO[11]; however the presented data in that study is unclear with no EXAFS fitting result to support the claim that Zn metal had formed.

The interatomic distance of the Zn metal determined by modeling (2.51 ± 0.2 Å) is contracted when compared to the theoretical distance of 2.67 Å for bulk Zn^0. A possible explanation of the bond distance contraction could be due to the nanosized nature of the Zn^0 particles, which were estimated to be ~0.8 nm from the fitted coordination number.[58] The interatomic distance of metallic nanoparticles has been observed to be less than the bulk material for various metals including Cu,[59] Ni,[59] Au,[60] Pd[61] and the nearest neighbor distance R has been reduced relative to the bulk by up to 10%.[62] Another possible explanation for the observed contraction in Zn-Zn interatomic distance could be due to the existence of a LiZn alloy which could allow a decreased Zn-Zn bond distance due to the introduction of Li ions. LiZn alloy has been recognized to form at voltages of ~0.157 V vs. Li/Li^+.[63, 64]

EXAFS spectra of the delithiated $ZnFe_2O_4$ electrode show that the initial spinel structure is not recovered. At the Fe edge, modeling indicates that the local atomic environment consists

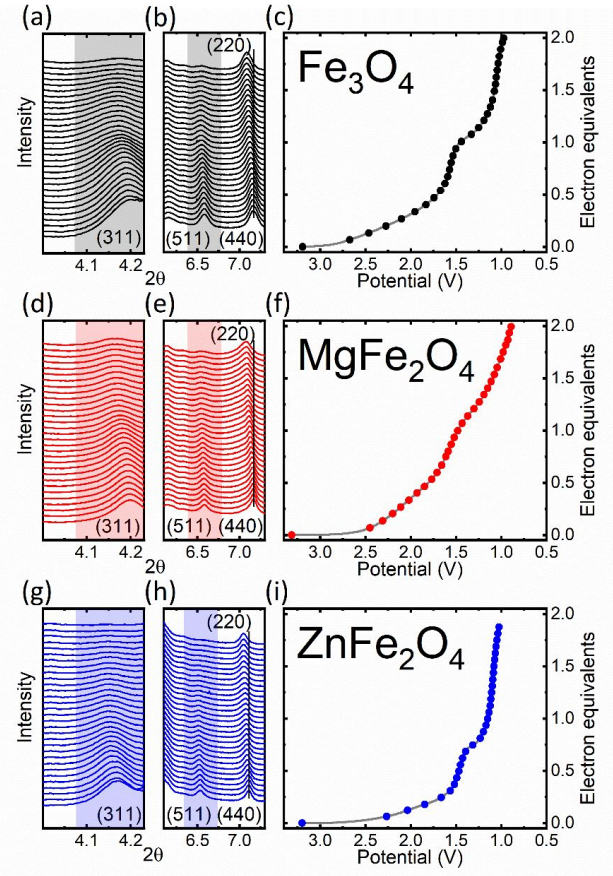

Figure 9. *Operando* synchrotron XRD electrochemistry of (a) Fe_3O_4, (d) $MgFe_2O_4$, and (c) $ZnFe_2O_4$ with corresponding (b, e, h) (311) and (c, f, i) (511)/(440) peaks, respectively.

of a FeO-like phase with similar Fe-O and Fe-Fe interatomic distances as delithiated Fe_3O_4 and $MgFe_2O_4$. Again, the number of near neighbors is significantly reduced compared to bulk FeO, indicating that the charged phase is amorphous or highly nanocrystalline. At the Zn edge, the data was fit using ZnO. Nearest neighbor Zn-O paths were determined from the fit at 1.96 ± 0.01 Å and 3.76 ± 0.03 Å with a Zn-Zn path at 3.21 ± 0.2 Å, in excellent agreement with the theoretical structure for hexagonal wurtzite, ZnO. No nearest neighboring Fe atoms were observed. Thus, EXAFS analysis indicates that the delithiation of $ZnFe_2O_4$ results in segregated FeO-like and ZnO phases. Previous XAS studies on $ZnFe_2O_4$ either did not study recharge of the material, [10] or found only small changes in the Zn and Fe spectra[11], indicating poor reversibility and in contrast to the results presented herein. A previous in-situTEM study of a graphene-$ZnFe_2O_4$ composite indicated that ZnO and Fe_2O_3 were the delithiated phases[65], however liquid electrolyte was not used in the setup, preventing the formation of SEI that may influence the delithiation process and reversibility.[66, 67] The results presented here indicate that further cycling after cycle 1 involves separate Zn oxide and Fe oxide phases.

X-ray Diffraction

Operando synchrotron XRD was collected on the three ferrite materials and the electrochemistry and corresponding XRD patterns are displayed in **Figure 9**. The data from the three spinel ferrite peaks corresponding to (311), (511), and (440)

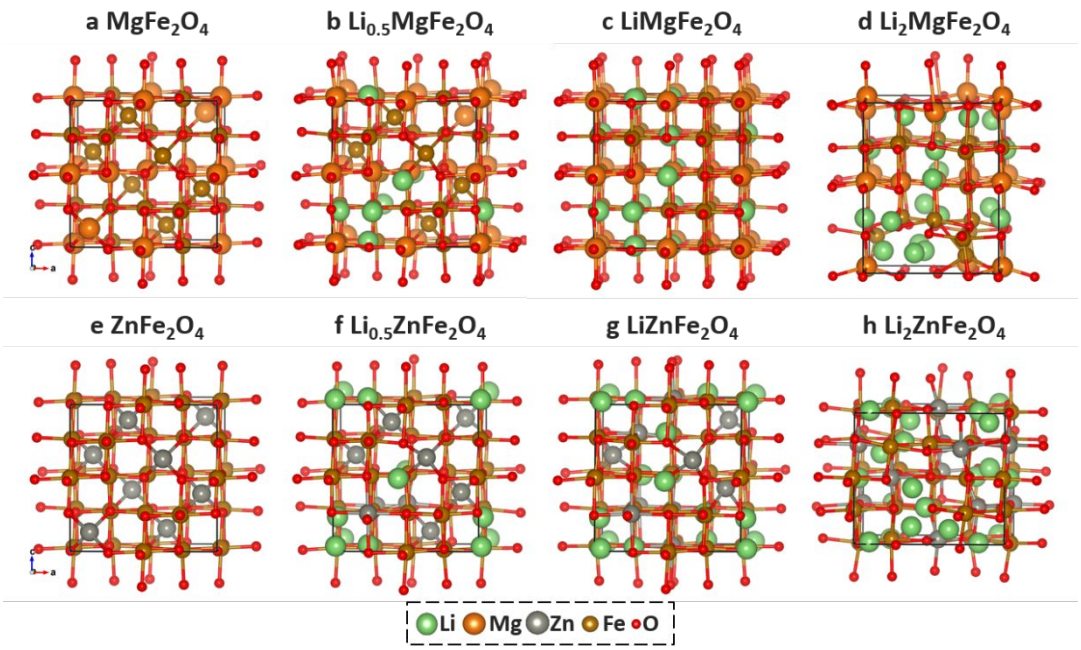

Figure 10. Structures of pristine mixed-spinel (a) $MgFe_2O_4$, (b) $Li_{0.5}MgFe_2O_4$, (c) rock-salt like $LiMgFe_2O_4$, (d) $Li_2MgFe_2O_4$ and (e) pristine spinel $ZnFe_2O_4$, (f) $Li_{0.5}ZnFe_2O_4$ (g) $LiZnFe_2O_4$ (h), $Li_2ZnFe_2O_4$.

reflections are shown. The data collected over the expanded 2-theta range are presented in **Figure S3.**

The (511) and (440) peaks were selected from the *operando* XRD datasets to track throughout the 2 ee discharge as they are intense and not convoluted with Li metal peaks. During discharge, the (511) peak gradually decreases, while the (440) peak gradually shifts to lower angle indicating a significant phase change occurs continuously. Analysis of (511) and (440) peaks provides insight into the onset and extent of phase transformation (**Figure S4**). Peak areas were normalized by the Cu (200) peak area to correct for the measured intensity variability of inactive pouch cell components and then normalized to 1 to account for small differences in the crystallinity of the three samples. The intensity of the (511) peak diminishes at a depth of discharge for all three ferrites through ~1.5 electron equivalents. Beyond 1.5 ee, the intensity of the $ZnFe_2O_4$ peak diminishes such that the peak area can no longer be distinguished. The area of the (440) peak remains constant for all three materials with increasing lithium content. During the lithiation process the (440) peak shifts to higher *d*-spacing as lattice expansion occurs. The d-spacing estimated from the (440) peak increases by 1.14 %, 1.29 %, and 0.84 %for Fe_3O_4, $MgFe_2O_4$, and $ZnFe_2O_4$, respectively.

DFT Calculations

Previous reports of density functional theory calculations for the lithiation of Fe_3O_4 provide support for the finding that Fe cation displacement from 8a to 16c site occurs during the first two electron equivalents of lithiation of the material.[4, 68] Vacant 16c octahedral sites in the structure are the most energetically favorable for the insertion of additional charge into the pristine Fe_3O_4.[68] However, Li^+ located in the 16c site are adjacent to two nearest neighboring Fe^{3+} cations in 8a sites with distance of only 1.8 Å, resulting in electrostatic repulsion. While at low levels of lithiation this repulsion does not result in structural change, above a critical lithium concentration, the electrostatic force displaces Fe^{3+} ions in 8a sites into adjacent empty 16c sites.[4, 68] DFT+U geometry optimization of the inverse spinel starting structure with insertion of one Li^+ equivalent in the 16c site predicts high lattice distortion, with the distance between neighboring Li_{16c}^+ and Fe_{8a}^{3+} elongated to 2.5 Å.[4] Instead, the most energetically favorable configuration predicted a mixture of Li and Fe ions occupying the 16c sites at 1 lithium insertion equivalent.[4] In further work, DFT calculations were used to probe the phase change and the concentration that it occurs in distinct structural organizations of Li and Fe cations in the Li-Fe-O ternary space for $Li_xFe_3O_4$ with x = 1.33.[68] This report predicted full displacement of iron 8a to 16c by x = 1.[68] DFT simulation of $Li_2Fe_3O_4$ predicts that Fe ions are no longer present in 8a sites and instead redistribute between 16c and 16d sites, resulting in equal occupation of 16c (3/4 sites occupation) and 16d (3/4 site occupation) sites.[4] This theoretical prediction is in good agreement with our EXAFS results, which show complete migration from 8a to 16c sites by two electron equivalents of reduction.

In this report we present DFT calculations to describe the lithiation intermediate, $Li_xAFe_2O_4$ (A=Zn, Mg) in the zinc ferrite and magnesium ferrite systems to gain an atomic level understanding of a phase transition from spinel to rock-salt like structure during the initial discharge process. For $MgFe_2O_4$, based on the refinement of the synchrotron XRD results, a mixed spinel starting structure with the tetrahedral 8a sites occupied by 75% Fe^{3+} ions and 25% Mg^{2+} ions and the octahedral 16d sites occupied by 62.5% Fe^{3+} ions and 37.5% Mg^{2+} ions was chosen to describe the pristine $MgFe_2O_4$ (**Figure 10a**). The DFT-optimized bond distances including Fe or Mg_{tet}- $Fe(Mg)_{tet}$ (3.70 ± 0.10 Å), $Fe(Mg)_{tet}$- $Fe(Mg)_{oct}$ (3.54 ± 0.10 Å), $Fe(Mg)_{oct}$-$Fe(Mg)_{oct}$ (3.02 ± 0.10 Å), $Fe(Mg)_{tet}$-O (1.93 ± 0.10 Å) and $Fe(Mg)_{oct}$-O (2.03 ± 0.10 Å) (**Figure S5**) from DFT calculations also agree with the EXAFS modeling results (**Figure 7**).

A systematic study of the discharge intermediates within 2 ee was carried out via a sequential Li^+ insertion into the cubic spinel

$MgFe_2O_4$	Tetrahedral Mg	Octahedral Mg	Tetrahedral Fe	Octahedaral Fe
Unlithiated	0.25	0.75	0.75	1.25
0.5 e^- lithiation	0.125	0.875	0.625	1.375
1 e^- lithiation	0	1	0	2
2 e^- lithiation	0	1	0	2
$ZnFe_2O_4$	Tetrahedral Zn	Octahedral Zn	Tetrahedral Fe	Octahedral Fe
Unlithiated	1	0	0	2
0.5 e^- lithiation	0.75	0.25	0	2
1 e^- lithiation	0.5	0.25	0	2
2 e^- lithiation	0	1	0	2

Table 1. DFT predicted content of tetrahedral and octahedral cations in $MgFe_2O_4$ and $ZnFe_2O_4$ at various lithiation stages. The total amount of Mg, Zn, Fe is calibrated to 1, 1, 2, respectively.

$MgFe_2O_4$ (**Figure 10a~d**). The initial lithiation starts with Li^+ insertion into the 16c vacancy. At 0.5 ee, due to the strong electrostatic repulsion from lateral Li^+ ions, 12.5% Mg^{2+} ions at the 8a sites migrate to the 16c vacancies, while the tetrahedral Fe^{3+} ions remain in the original 8a sites (**Figure 10b**, E_f = -1.49 eV/Li, **Table 1**). This finding is in good agreement with the EXAFS modeling results in **Figure 8**, which indicate an increase in the amplitude of Fe_{oct}-Mg coordinates with that of Fe_{tet}-Fe_{tet} unchanged at 0.5 ee. Further, Mg^{2+} displacement is more preferred at that stage over Fe^{3+} displacement, due to the higher affinity of Mg^{2+} to O ions in octahedral sites. Accordingly, $LiMgFe_2O_4$ displays a lower 8a site occupancy than $LiFe_3O_4$. At 1 ee, the DFT calculations predict a complete displacement of cations from 8a to 16c site together with a structural transformation to the rock-salt like structure (**Figure 10c**, E_f = -2.24 eV/Li, **Table 1**); while complete transformation by EXAFS is not observed until 2 ee. The discrepancy may be caused by inhomogeneity in discharge experimentally, where higher levels of discharge occur in the near surface region, while the deep core remains intact. The relatively low Li^+ concentration may hinder the diffusion toward the bulk. Upon going from 1 ee to 2 ee, both DFT and experiments observe the 100% tetrahedron → octahedron displacement (**Figure 10d**, E_f = -1.24 eV/Li, **Table 1**).

At higher discharge, according to our DFT calculations, full discharge ($MgFe_2O_4$ + 6 Li → MgO + 2 Fe + 3 Li_2O) to 6 ee releases the energy of 2.51 eV/Li. The distances of Fe-Fe in the formed metallic Fe bulk is estimated to be 2.45 ± 0.05 Å, in agreement with 2.54 ± 0.02 Å from EXAFS. By comparison a further discharge to 6 ee with the formation of metallic Mg ($MgFe_2O_4$ + 8 Li → Mg + 2 Fe + 4 Li_2O) is less preferred by 0.61 eV/Li. Both FeO and MgO adopt the rock salt structure with Fe^{2+} and Mg^{2+} cations having similar ionic radii in six-fold coordination (r_{Mg} = 72 pm, r_{Fe} = 78 pm[69]), and thus both materials have similar lattice energies (reported experimental values are 3838 kJ/mol and 3855 kJ/mol for MgO and FeO, respectively[70]). However, when comparing the associated products of the conversion reaction, Mg^0 is a significantly stronger reducing agent compared to Fe^0 (the oxidation potentials of Mg^0 to Mg^{2+} and Fe^0 to Fe^{2+} are 2.37 V and 0.44 V vs. SHE, respectively[71]). Our DFT calculations indicate that the oxidation of Mg to MgO (Mg + Li_2O → MgO + 2 Li) only requires an energy of 0.09 eV/Li. Thus, the fully reduced Mg^0 state is thermodynamically difficult to achieve, in agreement with the experimental discharge profiles in Figure 2.

In comparison with $MgFe_2O_4$, a normal spinel structure was adopted for pristine $ZnFe_2O_4$ (**Figure 10e**) with all Zn^{2+} ions located at the 8a site based on the synchrotron XPD. The discharge of $ZnFe_2O_4$ is mostly similar to $MgFe_2O_4$ and the detailed mechanisms have been demonstrated in our previous work.[10, 37, 38] Similar variations in bond distance of Zn_{tet}-O, Zn_{tet}-Zn_{tet}, Zn_{tet}-Fe_{oct}, Fe_{oct}-O and Fe_{oct} - Fe_{oct} during the discharge process of $ZnFe_2O_4$ is observed as seen in the case of $MgFe_2O_4$ (**Figure S5)**. In pristine $ZnFe_2O_4$, the distance of Zn_{tet}-Fe_{oct} is determined to be 3.54 ± 0.10 Å, in alignment with EXAFS (3.47 ± 0.01 Å and 3.50 ± 0.02 Å from Fe edge and Zn edge, respectively). An increase in the bond lengths is observed during the lithiation process within 2 ee. Further, the displacement of tetrahedral Zn^{2+} ions results in the decrease in the number of Zn_{tet}-O, Zn_{tet}-Fe_{oct} and Zn_{tet}-Zn_{tet} coordinates, leading to the weakened relative amplitude of the peaks in EXAFS (**Figure 8**). At 4 electron equivalents, Fe^{2+} ions were partially reduced to metallic Fe, as was observed in $MgFe_2O_4$. Upon further lithiation to 6 ee, Zn metal will form, for which the Zn-Zn bond length is 2.96 ± 0.05 Å. Here, we note that the calculations were performed at 0 K and the site preference may deviate when the entropic contribution was included. Nevertheless, in the current study, as demonstrated above, the optimized $Li_xAFe_2O_4$ structures agree reasonably well with the experimental measurements.

During the initial discharge process before 1 ee, the inserted Li^+ ions occupy the octahedral 16c vacancy sites, which is accompanied by the displacement of tetrahedral ions in AFe_2O_4 (A = Fe, Mg, Zn) from tetrahedral 8a to octahedral 16c sites. From 1 ee to 2 ee, Li^+ ions are inserted into less active tetrahedral 8a sites. Such preference for Li^+ ion insertion is universal for Fe_3O_4, $MgFe_2O_4$, and $ZnFe_2O_4$. However, the displacement of tetrahedral ion driven by Li^+ ion insertion in some aspect depends on the A cation in AFe_2O_4 (A = Fe, Mg, Zn). In $MgFe_2O_4$, the Mg^{2+}/Fe^{3+} ion migration starts at 0.125 ee and ends at 0.625 ee, resulting in a rock-salt like structure of $LiMgFe_2O_4$ with 100% tetrahedral ion displacement. In $ZnFe_2O_4$, the Zn^{2+} ion displacement starts at 0.25 ee and ends at 1.125 ee. Thus, $LiZnFe_2O_4$ processes an intermediate structure with 50% tetrahedral ion displacement. Besides the character of the A cation, these features can be also sensitive to applied current densities, particles sizes and shapes for spinel AFe_2O_4 according to previous studies.[10, 37, 38] That is, compared to Mg^{2+}/Fe^{3+}, Zn^{2+} ions prefer tetrahedral coordination in the spinel structure, in agreement with the previous study.[72] The strong preference of Zn^{2+} ions for tetrahedral coordination not only leads to the delay of tetrahedral ion displacement as demonstrated above, but also destabilizes the key lithiation intermediates. The formation energy of $LiZnFe_2O_4$ (-1.50 eV) is higher than that of $LiMgFe_2O_4$ (-2.24 eV), indicating that $LiZnFe_2O_4$ is less likely to form rock-salt like phase compared with $LiMgFe_2O_4$.

Previous hybrid DFT calculations for $LiNiFe_2O_4$ configurations at 1 ee[20] suggest that Li is not stable in the tetrahedral 8a site but that it is stabilized in open octahedral (16c or 16d) sites. These results suggest lithiation of the spinel structure is possible and

are in agreement with previous DFT calculations on Fe_3O_4 which predicted a mixture of Li and Fe ions occupying the 16c sites at 1 ee[4], as well as the calculations on $ZnFe_2O_4$ and $MgFe_2O_4$ presented herein, which also suggest lithiation at the 16c site.

Comparison of (de)lithiation mechanisms

Progression of discharge in Fe_3O_4, $MgFe_2O_4$ and $ZnFe_2O_4$ occurs by a similar mechanism, whereby the cation initially located in the tetrahedral (8a) site of the spinel structure migrates to the previously unoccupied octahedral 16c site after 2 electron equivalents of lithiation, resulting in a disordered rock salt like material. Since we observe this rearrangement in inverse spinel (Fe_3O_4), normal spinel ($ZnFe_2O_4$), and disordered spinel ($MgFe_2O_4$) structures, it is clear that the mechanism occurs whether the +2 cation or +3 cation is initially located in the 8a site. The structures of all three materials before and after this transition are shown in **Figure S6.**

The rearrangement of the spinel structure is supported by XANES, EXAFS, and DFT calculations. During the first 2 ee of lithiation, the XANES pre-edge 1s to 3d electronic transition features in Fe_3O_4 and $MgFe_2O_4$ reduce in intensity as Fe_{8a} ions move into centrosymmetric octahedral sites. In $ZnFe_2O_4$, this transition is not observed because Zn^{2+} ions occupy the 8a site in the normal spinel structure. Further indication of the 8a → 16c is given by the EXAFS results, where excellent fits of the 2 ee samples are obtained for all three materials when using a $[A]_{16c}[B_2]_{16d}O_4$ theoretical model. Notably, in each case the nearest neighbor oxygen distance is consistent with the spinel structure and considerably contracted compared to the nominal rock-salt FeO structure, suggesting rearrangement of cations within the spinel framework rather than formation of pure FeO (or ZnO in the case of $ZnFe_2O_4$) domains, as has been suggested in prior reports that used EXAFS modeling and XRD.[11, 17]

The displacement of cations from tetrahedral 8a to octahedral 16c sites during the lithiation process is anticipated to affect the ionic transport and reaction kinetics in the three materials. DFT calculations predict that in all three materials lithium insertion occurs initially into vacant 16c sites.[4, 68] After cation displacement of tetrahedral ions in AFe_2O_4 (A = Fe, Mg, Zn) to octahedral 16c sites, the most energetically favorable configuration is with Li and Fe cations occupying 16c sites.[4, 68] Because this process involves diffusion of both Li ions and A cations, the energy barrier for ionic transport during initial lithiation is anticipated to be high.[4] Post spinel to rock-salt like rearrangement, Li^+ conduction may occur by diffusion between adjacent 8a and 16c (now half occupied with A cations) sites, forming a facile three dimensional 8a-16c-8a pathway for ion transfer that is observed in Li based spinels.[73]

We note that in previous studies of lithiated $MnFe_2O_4$[74] and $MgFe_2O_4$[17], ^{7}Li MAS NMR data suggests formation of Li_2O formation by 2.0 ee. The NMR results are also in apparent disagreement with recent combined neutron and X-ray diffraction measurements of Fe_3O_4 at 2 ee, where the neutron diffraction is sensitive to Li occupancy and Li metal cation mixing.[75] The XRD and neutron data were refined with a two models: (a) a single lithiated spinel phase and (b) a mixture of lithiated spinel, FeO (rock-salt) and Li_2O phases. The best model for the data was the single lithiated spinel phase, where phases incorporating Li_2O and FeO resulted in missing reflections in the neutron data.[75] We hypothesize that possible differences between the reports may be due to lithiation approaches, since kinetic restrictions can result in significant polarization in the spinel ferrite based electrodes.[75-77] In the combined XRD/neutron study, experiments were performed at very low rates (C/600) to be close to equilibrium conditions, while in the NMR studies lithiation took place at a significantly faster C/20 rate. In the current study, we used low loading and low rate (C/30) to minimize polarization.

Lithiation beyond 2 ee occurs via conversion reaction, with simultaneous decrease of the $[A]_{16c}[B_2]_{16d}O_4$ phase and growth of Fe^0 and, in the case of $ZnFe_2O_4$, Zn^0 as well. In the fully lithiated state, EXAFS spectrum could be modeled using only Fe-Fe_{metal} paths for Fe_3O_4 and $MgFe_2O_4$, while for discharged $ZnFe_2O_4$ both Zn_{metal} and an oxide phase were needed to effectively fit the data due to the greater oxidizing strength of Fe^{2+} vs. Zn^{2+}. The metal nanoparticles formed in each case showed small sizes from 0.8 – 1.0 nm estimated from fitted coordination numbers.

Delithiation of all three materials results in formation of an iron oxide phase characterized by (1) reduced first shell Fe-O interatomic distance compared to either the $Li_2[A]_{16c}[B_2]_{16d}O_4$ phase during lithiation or the nominal FeO structure, (2) very low relative amplitudes for all nearest neighboring atoms, and (3) a second Fe-O path above 3 Å. These data suggest that the charged oxide is not bulk FeO but rather a disordered nanocrystalline phase. This assertion is supported by the emergence of a pre-edge peak in the XANES spectra, which indicates that the Fe-atoms are in a coordination environment without centrosymmetric symmetry, rather than a purely octahedral environment as in rock-salt FeO. The analysis suggests that the delithiated state consists of FeO domains, where oxidized Fe atoms on the surfaces of the particle increase the average oxidation state of the iron and distort the Fe site symmetry from an octahedral geometry. For the charged $ZnFe_2O_4$ electrode, ZnO is observed with interatomic distances that are in excellent agreement with the hexagonal wurtzite structure. Notably, no Fe-Zn paths could be modeled, indicating distinct separation of FeO and ZnO domains.

Conclusions

XAS, operando synchrotron XRD measurements, and DFT calculations were used to provide insight into the (de)lithiation processes of three spinel ferrites with different +2 cations: Fe_3O_4, $MgFe_2O_4$, and $ZnFe_2O_4$. The study represents a mechanistic comparison of three spinel ferrite types (inverse, normal, partially inverse) with similar crystallite size and electrochemical test conditions. The results provide insight into the electrochemical (de)lithiation mechanisms of the spinel ferrites and highlight the benefit of combined spectroscopic, diffraction and theoretical analyses to elucidate reaction mechanisms.

The study reveals that at the initial discharge stage the Li^+ ion insertion follows a similar mechanism for normal, inverse, and partially inverse spinels independent of the +2 cation type. In each case, the lithiation mechanism proceeds via a $[A]_{16c}[B_2]_{16d}O_4$ phase with partially occupied 16c sites, where cations rearrange within the spinel framework rather than form pure FeO (or ZnO in the case of $ZnFe_2O_4$) domains.

Upon delithiation, the Fe-atoms are in a coordination geometry with low inversion symmetry where a significant fraction of the

oxidized Fe atoms are in an environment that is distorted from a purely octahedral geometry expected in a rock-salt structure. The results are consistent with amorphous FeO domains, where oxidized Fe atoms on the surfaces of the particle increase the average oxidation state of the iron and distort the Fe site symmetry from an octahedron. The spinel ferrites with other transition metal +2 cations ($MgFe_2O_4$, $ZnFe_2O_4$) show phase segregation between the FeO-like phase and either MgO- or ZnO-like domains in the charged state, as determined by local atomic structure analysis of EXAFS data. The observed segregation of phases demonstrates that the substitution of 2^+ cation has a significant impact on the nature of the delithiated phase(s) in this class of iron oxide materials.

Conflicts of interest

There are no conflicts to declare.

Acknowledgements

This work was supported as part of the Center for Mesoscale Transport Properties, an Energy Frontier Research Center supported by the U.S. Department of Energy (DOE), Office of Science, Basic Energy Sciences, under award #DE-SC0012673. XAS measurements used the resources of the Advanced Photon Source, a DOE, Office of Science User Facility operated for the DOE Office of Science by Argonne National Laboratory under Contract No. DE-AC02-06CH11357. The synchrotron-based XPD data were collected at the National Synchrotron Light Source II, Brookhaven National Laboratory, which is supported by the Department of Energy, under Contract No. DE-SC0012704. The DFT calculations were performed using computational resources at the Center for Functional Nanomaterials, which is a U.S. DOE Office of Science Facility, and the Scientific Data and Computing Center, a component of the BNL Computational Science Initiative, at Brookhaven National Laboratory, which is supported by the Department of Energy, under Contract No. DE-SC0012704. M.M.H. and A.M.B. acknowledge that this material is based upon work supported by the National Science Foundation Graduate Research Fellowship Program under Grant No. 1109408. D.M.L. acknowledges support from the National Science Foundation funded ExCELS Research Experience for Undergraduates under award 1358959. A.H.M. acknowledges support from the National Science Foundation funded Research Experience for Undergraduates: Nanotechnology for Health, Energy and the Environment under award 1659657. EST acknowledges support from the William and Jane Knapp Chair in Energy and the Environment.

References

1. A. M. Bruck, C. A. Cama, C. N. Gannett, A. C. Marschilok, E. S. Takeuchi and K. J. Takeuchi, *Inorg. Chem. Front.*, 2016, **3**, 26-40.
2. M. M. Thackeray, W. I. F. David and J. B. Goodenough, *Mater. Res. Bull.*, 1982, **17**, 785-793.
3. D. C. Bock, C. J. Pelliccione, W. Zhang, J. Timoshenko, K. W. Knehr, A. C. West, F. Wang, Y. Li, A. I. Frenkel, E. S. Takeuchi, K. J. Takeuchi and A. C. Marschilok, *Phys. Chem. Chem. Phys.*, 2017, **19**, 20867-20880.
4. W. Zhang, D. C. Bock, C. J. Pelliccione, Y. Li, L. Wu, Y. Zhu, A. C. Marschilok, E. S. Takeuchi, K. J. Takeuchi and F. Wang, *Adv. Energy Mater.*, 2016, **6**, 1502471.
5. Y. Huang, Z. H. Xu, J. Q. Mai, T. K. Lau, X. H. Lu, Y. J. Hsu, Y. S. Chen, A. C. H. Lee, Y. L. Hou, Y. S. Meng and Q. Li, *Nano Energy*, 2017, **41**, 426-433.
6. J. Y. Ma, X. T. Guo, Y. Yan, H. G. Xue and H. Pang, *Adv. Sci.*, 2018, **5**, 28.
7. S. J. Yu, V. M. H. Ng, F. J. Wang, Z. H. Xiao, C. Y. Li, L. B. Kong, W. X. Que and K. Zhou, *J. Mater. Chem. A*, 2018, **6**, 9332-9367.
8. X. Guo, X. Lu, X. Fang, Y. Mao, Z. Wang, L. Chen, X. Xu, H. Yang and Y. Liu, *Electrochem. Commun.*, 2010, **12**, 847-850.
9. Y. Pan, Y. Zhang, X. Wei, C. Yuan, J. Yin, D. Cao and G. Wang, *Electrochim. Acta*, 2013, **109**, 89-94.
10. Y. Zhang, C. J. Pelliccione, A. B. Brady, H. Guo, P. F. Smith, P. Liu, A. C. Marschilok, K. J. Takeuchi and E. S. Takeuchi, *Chem. Mater.*, 2017, **29**, 4282-4292.
11. D. Zhou, H. Jia, J. Rana, T. Placke, T. Scherb, R. Kloepsch, G. Schumacher, M. Winter and J. Banhart, *Electrochim. Acta*, 2017, **246**, 699-706.
12. Y.-N. NuLi, Y.-Q. Chu and Q.-Z. Qin, *J. Electrochem. Soc.*, 2004, **151**, A1077-A1083.
13. Y. Sharma, N. Sharma, G. V. S. Rao and B. V. R. Chowdari, *Electrochim. Acta*, 2008, **53**, 2380-2385.
14. P. F. Teh, Y. Sharma, S. S. Pramana and M. Srinivasan, *J. Mater. Chem.*, 2011, **21**, 14999-15008.
15. S. Yagi, Y. Ichikawa, I. Yamada, T. Doi, T. Ichitsubo and E. Matsubara, *Jpn. J. Appl. Phys.*, 2013, **52**, 025501/025501-025501/025506.
16. N. Sivakumar, S. R. P. Gnanakan, K. Karthikeyan, S. Amaresh, W. S. Yoon, G. J. Park and Y. S. Lee, *J. Alloys Compd.*, 2011, **509**, 7038-7041.
17. S. Permien, S. Indris, M. Scheuermann, U. Schuermann, V. Mereacre, A. K. Powell, L. Kienle and W. Bensch, *J. Mater. Chem. A*, 2015, **3**, 1549-1561.
18. G. Balachandran, D. Dixon, N. Bramnik, A. Bhaskar, M. Yavuz, L. Pfaffmann, F. Scheiba, S. Mangold and H. Ehrenberg, *ChemElectroChem*, 2015, **2**, 1510-1518.
19. S. Permien, S. Indris, A.-L. Hansen, M. Scheuermann, D. Zahn, U. Schürmann, G. Neubüser, L. Kienle, E. Yegudin and W. Bensch, *ACS Appl. Mater. Interfaces*, 2016, **8**, 15320-15332.
20. S. Permien, T. Neumann, S. Indris, G. Neubüser, L. Kienle, A. Fiedler, A.-L. Hansen, D. Gianolio, T. Bredow and W. Bensch, *Phys. Chem. Chem. Phys.*, 2018, **20**, 19129-19141.
21. D. Zhou, S. Permien, J. Rana, M. Krengel, F. Sun, G. Schumacher, W. Bensch and J. Banhart, *J. Power Sources*, 2017, **342**, 56-63.
22. S. Zhu, A. C. Marschilok, E. S. Takeuchi, G. T. Yee, G. Wang and K. J. Takeuchi, *J. Electrochem. Soc.*, 2010, **157**, A1158-A1163.
23. B. Ravel and M. J. Newville, *J. Synchrotron Radiat.*, 2005, **12**, 537-541.
24. J. J. Rehr, J. Mustre de Leon, S. I. Zabinsky and R. C. Albers, *J. Am. Chem. Soc.*, 1991, **113**, 5135.
25. M. E. Fleet, *Acta Crys.*, 1984, **40**, 1491-1493.
26. F. A. López, A. López-Delgado, J. L. Martín de Vidales and E. Vila, *J. Alloys Compd.*, 1998, **265**, 291-296.
27. E. A. Owen and E. L. Yates, *Philos Mag*, 1933, **15**, 472-488.
28. H. E. Swanson and E. Tatge, *Natl. Bur. Stand. Circ. (U. S.)*, 1953, **539**, 95 pp.

29. B. H. Toby and R. B. Von Dreele, *J. Appl. Crystallogr.*, 2013, **46**, 544-549.
30. G. Kresse and J. Hafner, *Phys. Rev. B*, 1994, **49**, 14251-14269.
31. G. Kresse and J. Furthmüller, *Phys. Rev. B*, 1996, **54**, 11169-11186.
32. V. I. Anisimov, J. Zaanen and O. K. Andersen, *Phys. Rev. B*, 1991, **44**, 943-954.
33. V. I. Anisimov, F. Aryasetiawan and A. I. Lichtenstein, *J. Phys. Condens. Matter*, 1997, **9**, 767-808.
34. P. E. Blöchl, *Phys. Rev. B*, 1994, **50**, 17953-17979.
35. G. Kresse and D. Joubert, *Phys. Rev. B*, 1999, **59**, 1758-1775.
36. J. P. Perdew, K. Burke and M. Ernzerhof, *Phys. Rev. Lett.*, 1996, **77**, 3865-3868.
37. H. Guo, Y. Zhang, A. C. Marschilok, K. J. Takeuchi, E. S. Takeuchi and P. Liu, *Phys. Chem. Chem. Phys.*, 2017, **19**, 26322-26329.
38. H. Guo, A. C. Marschilok, K. J. Takeuchi, E. S. Takeuchi and P. Liu, *ACS Appl. Mater. Interfaces*, 2018, **10**, 35623−35630.
39. H. Guo, J. L. Durham, A. B. Brady, A. C. Marschilok, E. S. Takeuchi, K. J. Takeuchi and P. Liu, *J. Electrochem. Soc.*, 2020, **167**, 090506.
40. S. J. Mole, X. Zhou and R. Liu, *J. Phys. Chem.*, 1996, **100**, 14665-14671.
41. J. Nonkumwong, S. Ananta, P. Jantaratana, S. Phumying, S. Maensiri and L. Srisombat, *J Magn Magn Mater*, 2015, **381**, 226-234.
42. A. Loganathan and K. Kumar, *Appl. Nanosci.*, 2016, **6**, 629-639.
43. L. Zhao, M. M. Gao, W. B. Yue, Y. Jiang, Y. Wang, Y. Ren and F. Q. Hu, *ACS Appl. Mater. Interfaces*, 2015, **7**, 9709-9715.
44. M. M. Huie, D. C. Bock, L. Wang, A. C. Marschilok, K. J. Takeuchi and E. S. Takeuchi, *J. Phys. Chem. C*, 2018, **122**, 10316-10326.
45. M. M. Huie, D. C. Bock, A. M. Bruck, K. R. Tallman, L. M. Housel, L. Wang, J. Thieme, K. J. Takeuchi, E. S. Takeuchi and A. C. Marschilok, *ACS Appl. Mater. Interfaces*, 2019, **11**, 7074-7086.
46. S. H. Lee, S.-H. Yu, J. E. Lee, A. Jin, D. J. Lee, N. Lee, H. Jo, K. Shin, T.-Y. Ahn, Y.-W. Kim, H. Choe, Y.-E. Sung and T. Hyeon, *Nano Lett.*, 2013, **13**, 4249-4256.
47. S. J. Rezvani, R. Gunnella, A. Witkowska, F. Mueller, M. Pasqualini, F. Nobili, S. Passerini and A. D. Cicco, *ACS Appl. Mater. Interfaces*, 2017, **9**, 4570-4576.
48. D. C. Bock, C. J. Pelliccione, W. Zhang, J. Wang, K. W. Knehr, J. Wang, F. Wang, A. C. West, A. C. Marschilok, K. J. Takeuchi and E. S. Takeuchi, *ACS Appl. Mater. Interfaces*, 2016, **8**, 11418-11430.
49. M. D. Sharkov, M. E. Boiko, A. V. Bobyl, E. M. Ershenko, E. I. Terukov and Y. V. Zubavichus, *Crystallogr. Rep.*, 2013, **58**, 993-997.
50. T. Yamamoto, *X-Ray Spectrometry*, 2008, **37**, 572-584.
51. C. H. M. van Oversteeg, H. Q. Doan, F. M. F. de Groot and T. Cuk, *Chem. Soc. Rev.*, 2017, **46**, 102-125.
52. T. E. Westre, P. Kennepohl, J. G. DeWitt, B. Hedman, K. O. Hodgson and E. I. Solomon, *J. Am. Chem. Soc.*, 1997, **119**, 6297-6314.
53. R. A. Bair and W. A. Goddard, *Phys. Rev. B*, 1980, **22**, 2767-2776.
54. M. L. Baker, M. W. Mara, J. J. Yan, K. O. Hodgson, B. Hedman and E. I. Solomon, *Coord. Chem. Rev.*, 2017, **345**, 182-208.
55. M. Wilke, F. Farges, P.-E. Petit, G. E. Brown Jr and F. Martin, *Am. Mineral.*, 2001, **86**, 714-730.
56. R. G. Shulman, Y. Yafet, P. Eisenberger and W. E. Blumberg, *P Natl Acad Sci USA*, 1976, **73**, 1384-1388.
57. A. L. Roe, D. J. Schneider, R. J. Mayer, J. W. Pyrz, J. Widom and L. Que, *J. Am. Chem. Soc.*, 1984, **106**, 1676-1681.
58. S. Calvin, M. M. Miller, R. Goswami, S. F. Cheng, S. P. Mulvaney, L. J. Whitman and V. G. Harris, *J. Appl. Phys.*, 2003, **94**, 778-783.
59. G. Apai, J. F. Hamilton, J. Stohr and A. Thompson, *Phys. Rev. Lett.*, 1979, **43**, 165-169.
60. J. T. Miller, A. J. Kropf, Y. Zha, J. R. Regalbuto, L. Delannoy, C. Louis, E. Bus and J. A. van Bokhoven, *J. Catal.*, 2006, **240**, 222-234.
61. C. M. Lin, T. L. Hung, Y. H. Huang, K. T. Wu, M. T. Tang, C. H. Lee, C. T. Chen and Y. Y. Chen, *Phys. Rev. B*, 2007, **75**, 125426/125421-125426/125426.
62. A. Yevick and A. I. Frenkel, *Phys. Rev. B*, 2010, **81**, 115451.
63. J. Wang, P. King and R. A. Huggins, *Solid State Ionics*, 1986, **20**, 185-189.
64. Y. Hwa, J. H. Sung, B. Wang, C.-M. Park and H.-J. Sohn, *J. Mater. Chem.*, 2012, **22**, 12767-12773.
65. Q. Su, S. Wang, L. Yao, H. Li, G. Du, H. Ye and Y. Fang, *Sci. Rep.*, 2016, **6**, 28197.
66. Y. Wu and N. Liu, *Chem*, 2018, **4**, 438-465.
67. D. C. Bock, G. H. Waller, A. N. Mansour, A. C. Marschilok, K. J. Takeuchi and E. S. Takeuchi, *The Journal of Physical Chemistry C*, 2018, **122**, 14257-14271.
68. C. N. Lininger, C. A. Cama, K. J. Takeuchi, A. C. Marschilok, E. S. Takeuchi, A. C. West and M. S. Hybertsen, *Chem. Mater.*, 2018, **30**, 7922-7937.
69. R. D. Shannon, *Acta Crystallogr., Sect. A*, 1976, **32**, 751-767.
70. S. Kaya and C. Kaya, *Inorg. Chem.*, 2015, **54**, 8207-8213.
71. W. M. Haynes, D. R. Lide and T. J. Burno, eds., *CRC Handbook of Chemistry and Physics: a ready-reference book of chemical and physical data*, CRC Press, Boca Raton, FL, 2016.
72. K. Shimokawa, T. Atsumi, M. Harada, R. E. Ward, M. Nakayama, Y. Kumagai, F. Oba, N. L. Okamoto, K. Kanamura and T. Ichitsubo, *J. Mater. Chem. A*, 2019, **7**, 12225-12235.
73. B. Xu and S. Meng, *J. Power Sources*, 2010, **195**, 4971-4976.
74. S. Permien, H. Hain, M. Scheuermann, S. Mangold, V. Mereacre, A. K. Powell, S. Indris, U. Schürmann, L. Kienle, V. Duppel, S. Harm and W. Bensch, *RSC Adv.*, 2013, **3**, 23001-23014.
75. C. N. Lininger, N. W. Brady and A. C. West, *Acc. Chem. Res.*, 2018, **51**, 583-590.
76. K. W. Knehr, N. W. Brady, C. A. Cama, D. C. Bock, Z. Lin, C. N. Lininger, A. C. Marschilok, K. J. Takeuchi, E. S. Takeuchi and A. C. West, *J. Electrochem. Soc.*, 2015, **162**, A2817-A2826.
77. K. W. Knehr, N. W. Brady, C. N. Lininger, C. A. Cama, D. C. Bock, Z. Lin, A. C. Marschilok, K. J. Takeuchi, E. S. Takeuchi and A. C. West, *ECS Trans.*, 2015, **69**, 7-19.

TOC Figure (8 cm x 4 cm):

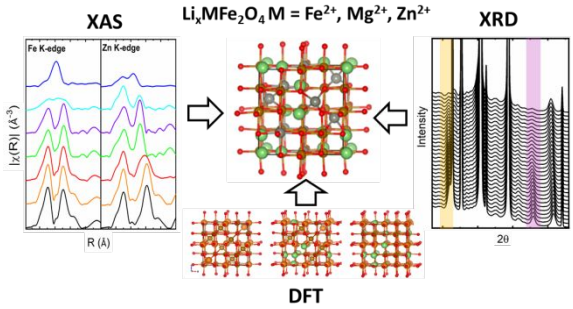

TOC Caption: Combined x-ray absorption spectroscopy, synchrotron X-ray diffraction, and density functional theory elucidate (de)lithiation mechanisms for the spinel ferrites MFe_2O_4 (M = Fe^{2+}, Mg^{2+}, Zn^{2+})